Microscale C-O-S isotope signatures record microbial sulfate reduction in ancient deep subsurface pyrite-calcite-barite assemblages

Eric Runge[1,2*], Vanessa Fichtner[1,3], Mikael Tillberg[1], Martin Whitehouse[4], Henrik Drake[1]

[1]Department of Biology and Environmental Science, Linnaeus University, Kalmar, Sweden
[2]GeoZentrum Nordbayern, Friedrich-Alexander-Universität (FAU) Erlangen-Nürnberg, Erlangen, Germany
[3]Department of Geobiology, University of Göttingen, Göttingen, Germany
[4]Laboratory for Isotope Geology, Swedish Museum of Natural History, Stockholm, Sweden

Correspondence to: Eric Runge (eric.runge@fau.de)

Abstract. The deep biosphere harbors diverse microbial communities amounting to a substantial fraction of Earth's biomass for much of its history. Analyses of fracture-hosted minerals (e.g., pyrite, calcite) and their C-O-S isotope signatures are beginning to establish a fossil record of subsurface microbial communities and their relationship with major geological events. Fracture-coating pyrite from deep within the Fennoscandian Shield records the largest ^{34}S-enrichment observed on Earth to date ($\delta^{34}S$ = +147 ‰) – likely the result of late-stage Rayleigh distillation during closed-system microbial sulfate reduction (MSR). This implies even heavier S isotope values for the complementary sulfate reservoir during pyrite formation, possibly recorded in coeval sulfate minerals such as barite [$BaSO_4$]. However, barite has been poorly explored as an archive of ancient deep subsurface biosignatures, particularly in samples with extreme ^{34}S-enrichment in pyrite. Here, we compiled published microscale $\delta^{13}C_{calcite}$, $\delta^{18}O_{calcite}$, and $\delta^{34}S_{pyrite}$ data with new secondary ion mass spectrometry (SIMS) $\delta^{18}O_{barite}$ and $\delta^{34}S_{barite}$ analyses from two localities on the Fennoscandian Shield (Forsmark and Laxemar, Southeastern Sweden), aiming to constrain the record of microbial processes in barite. We identified two groups of barites distinguished by their distinct $\delta^{18}O/\delta^{34}S$ trends. Comparison of these trends with $\delta^{13}C$ values of cogenetic calcite reveals variable associations with sulfate-dependent anaerobic oxidation of methane (AOM) and organotrophic sulfate reduction (OSR). Strongly ^{13}C-depleted calcite ($\delta^{13}C_{calcite} < -40$ ‰), indicating a relationship with AOM, almost exclusively occurs in the steeper-trending Group 1. Evidence for barite affected by OSR ($\delta^{13}C_{calcite} > -30$ ‰) occurs in both groups and dominates the shallower-trending Group 2. The different trends likely resulted from an interplay of MSR pathways (AOM vs. OSR) and variations in sulfate reduction rates (SRR), which we attribute to the relative abundances of sulfate and electron donors in the parent fluid of barite. Lower sulfate and electron donor abundances likely permitted methanogenesis and AOM at lower SRR, resulting in a steeper $\delta^{18}O/\delta^{34}S$ trend in Group 1 barite. Conversely, higher sulfate and electron donor abundances inhibited methanogenesis and AOM, favoring OSR at a higher SRR, which is reflected by the shallower $\delta^{18}O/\delta^{34}S$ trend in Group 2 barite. Comparison between the $\delta^{34}S_{pyrite}$ range (−53.9 to +131.7 ‰) and the $\delta^{34}S_{barite}$ range (+7.6 to +52.0 ‰) across both localities demonstrates that the sulfate reservoir corresponding to extremely ^{34}S-enriched pyrite is not recorded in barite. The discrepancy between barite and pyrite could reflect their formation in separate microenvironments or barite undersaturation at high degrees of Rayleigh distillation. Our study highlights the need for coupled microscale C-O-S analyses in fracture-hosted mineral assemblages to understand metabolic processes in the ancient deep biosphere, while stressing that these records are affected by local hydrogeochemical conditions.

1 Introduction

The average depth of the 122 °C isotherm in the continental crust is 4.8 km, defining a vast rock volume that is cooler than the upper known temperature limit of life (Takai et al., 2008). For this reason, fractures and rock pores in the continental crust represent one of the largest habitable environments on Earth (Magnabosco et al., 2018). This 'deep biosphere' hosts diverse communities of chemolithoautotrophic primary producers and heterotrophic microorganisms, including methanogens, methanotrophs, and sulfate reducers (Chivian et al., 2008; Kieft et al., 2018; Ruff et al., 2024; Stevens and McKinley, 1995; Wu et al., 2016). Recent estimates of the total biomass of the deep biosphere vary (Bar-On et al., 2018; Magnabosco et al., 2018; McMahon and Parnell, 2014), but its significant impact on global biogeochemical cycles is generally accepted. Before the rise of land plants, the deep subsurface may have even held the majority of Earth's total biomass (McMahon and Parnell, 2018). Indeed, portions of the continental crust have been continuously habitable since 1.1 billion years ago (Ga) and may have experienced habitable periods since 1.9 Ga (Drake and Reiners, 2021). Understanding the diversity and biogeochemical impact of the deep biosphere throughout Earth's history requires robust and geologically stable biosignatures. However, the deep biosphere fossil record remains patchy and poorly understood (Gustafsson and Drake, 2025; Ivarsson et al., 2020).

Minerals and their stable isotope ratios can represent valuable biosignatures in deep time (Runge et al., 2023). For instance, the largest magnitudes of S isotope fractionation between sulfate and sulfide ($^{34}\varepsilon = \delta^{34}S_{sulfate} - \delta^{34}S_{sulfide}$) are associated with kinetic isotope effects (KIE) during microbial sulfate reduction (MSR). Depending on the microbial strain and environmental parameters, such as the temperature, or the availability of sulfate and electron donors (organic matter or H_2), $^{34}\varepsilon$ induced by MSR can vary between 0 and ~70 ‰ (Bradley et al., 2016; Chambers et al., 1975; Farquhar et al., 2003; Habicht et al., 2002; Ries et al., 2009; Sim et al., 2011; Wing and Halevy, 2014; Wortmann et al., 2001). These signatures can be recorded in ^{34}S-depleted authigenic sulfide minerals (e.g., pyrite) (Halevy et al., 2023; Pasquier et al., 2025; Strauss, 1997). Microbial sulfate reduction can also be coupled with anaerobic oxidation of methane (AOM), which is well supported in the deep subsurface (Bell et al., 2022; Drake et al., 2015, 2017; Kotelnikova, 2002). Microbially produced methane is ^{13}C-depleted relative to CO_2 by up to 95 ‰ (Whiticar, 1999), hence methane oxidation via AOM can result in the precipitation of strongly ^{13}C-depleted calcite (Aloisi et al., 2002; Campbell et al., 2002; Feng et al., 2010; Lin et al., 2011; Natalicchio et al., 2012; Reitner et al., 2005). Calcite precipitation resulting from organotrophic sulfate reduction (OSR) typically reflects the less ^{13}C-depleted organic carbon substrate. Notably, dating of fracture-coating minerals (adularia Rb/Sr, calcite U/Pb, and hematite U-Th/He) co-genetic to biosignatures in pyrite and calcite records ancient MSR deep within the Fennoscandian Shield between the Ordovician (460 ± 30 Ma) and the Neogene (13.7 ± 0.6 Ma) (Drake et al., 2017, 2018, 2021). Thus, combining S and C isotope ratios is a powerful approach for reconstructing ancient MSR pathways.

During the early stages of MSR, $\delta^{18}O_{sulfate}$ increases via a minor KIE and an equilibrium isotope effect (EIE) between H_2O and intermediate S species (e.g., sulfite) before their re-oxidation to sulfate (Antler et al., 2013; Böttcher et al., 1999; Brunner et al., 2005; Fritz et al., 1989; Mizutani and Rafter, 1973; Wortmann et al., 2007) (Fig. 1). The slopes of $\delta^{18}O/\delta^{34}S$ trends are strongly controlled by the sulfate reduction rate (SRR). At a lower SRR, the equilibration of intermediate S species with water

is more pronounced, and $\delta^{18}O_{sulfate}$ rises more rapidly relative to $\delta^{34}S_{sulfate}$ (i.e., a steeper slope). At a higher SRR, the rise in $\delta^{18}O_{sulfate}$ relative to $\delta^{34}S_{sulfate}$ is less pronounced (i.e., a shallower slope). In addition, AOM and OSR can result in different slopes at similar SRR (Antler et al., 2014), and the slopes resulting from AOM differ between methane diffusion-limited settings (e.g., marine sediments: steeper trend) and methane-in-excess environments (e.g., cold seeps, stratified estuaries: shallower trend) (Antler et al., 2015) (Fig. 1). Owing to the preferential consumption of $^{32}SO_4^{2-}$ by microorganisms, MSR in a closed system (i.e., when the SRR exceeds the resupply of sulfate) can produce ^{34}S-enriched sulfate in the residual porewater (Anderson et al., 1987; Jørgensen et al., 2004; Rudnicki et al., 2001; Zaback et al., 1993). This process has resulted in $\delta^{34}S_{pyrite}$ values of up to +147 ‰ in deep fractures of the Fennoscandian Shield, the most extreme ^{34}S-enrichment yet reported (Drake et al., 2018). This implies an even more ^{34}S-enriched complementary sulfate reservoir during pyrite formation. Barite [$BaSO_4$] is a robust archive of $\delta^{18}O_{sulfate}$ and $\delta^{34}S_{sulfate}$ values in its parent fluid because its precipitation is associated with minimal stable isotope fractionation and it is thermodynamically stable and poorly soluble (Crockford et al., 2019; Griffith and Paytan, 2012; Han et al., 2025; Paytan et al., 1998, 2002; Turchyn and Schrag, 2004, 2006; Wood et al., 2021). Thus, the co-variation of $\delta^{18}O_{barite}$ and $\delta^{34}S_{barite}$ values may record past and extant environmental conditions and microbial S cycling, complementing the C-O-S isotope records in pyrite and calcite. However, pyrite-calcite-barite assemblages are poorly explored archives of ancient deep subsurface microbial processes, particularly in samples containing extremely ^{34}S-enriched pyrite.

Here, we compile previously published microscale $\delta^{13}C_{calcite}$, $\delta^{18}O_{calcite}$, and $\delta^{34}S_{pyrite}$ data from multiple deep drill cores taken at two localities on the Fennoscandian Shield (Forsmark and Laxemar/Äspö, Southeastern Sweden) with new secondary ion mass spectrometry (SIMS) $\delta^{18}O_{barite}$ and $\delta^{34}S_{barite}$ analyses from the same drill cores. In most cases, barite occurred in fractures that contained associated pyrite and/or calcite. Although we did not detect extreme ^{34}S-enrichment in barite, our results demonstrate that barite records an ancient archive of OSR and AOM, while highlighting that these archives are affected by local hydrogeochemical conditions.

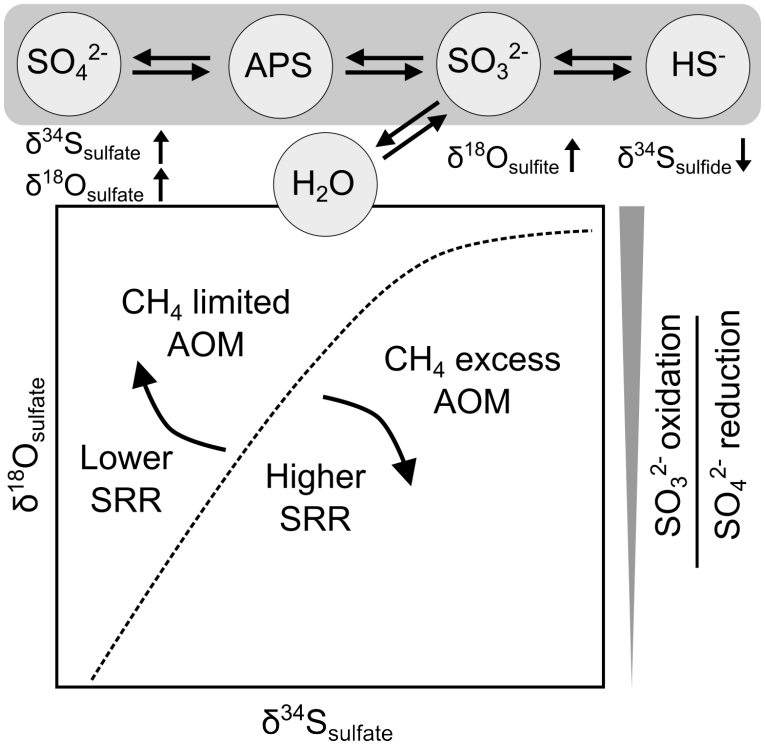


Figure 1: Controls on $\delta^{18}O/\delta^{34}S$ trends during the early stages of microbial sulfate reduction (MSR). The intracellular reduction of sulfate to sulfide (HS^-) proceeds via multiple reversible steps, including the activation of adenosine 5′-phosphosulfate (APS) and reduction to sulfite (SO_3^2). The kinetic isotope effect (KIE) associated with MSR produces ^{34}S-depleted sulfide and ^{34}S-enriched residual sulfate. Concerning O, the KIE associated with MSR is small, and the equilibrium isotope exchange (EIE) between sulfate and water is kinetically inhibited. However, intermediate S species such as sulfite readily exchange O isotopes with water and become relatively ^{18}O-enriched. Intracellular re-oxidation of this sulfite produces ^{18}O-enriched sulfate. The $\delta^{18}O/\delta^{34}S$ trends in residual sulfate are controlled by the expression of the EIE associated with sulfite-water exchange relative to the sulfate reduction rate (SRR). This expression becomes more pronounced when the SRR is lower, or when anaerobic oxidation of methane (AOM) occurs under methane (CH_4) limited conditions, resulting in a steeper slope. After Wortmann et al. (2007), Antler et al. (2013, 2014, 2015), Han et al. (2025).

2 Methods

2.1 Materials and sampling

The sampled barite-bearing fractures are from Proterozoic crystalline bedrock at Forsmark, Laxemar, and Äspö (Southeastern Sweden) (see Drake et al. (2018) for details on the geological setting). Laxemar and Äspö are situated on the Baltic Sea coastline, and only ca. three kilometers apart; hence we consider them as one site (i.e., Laxemar) in this study. Drill cores were mainly obtained by triple-tube drilling conducted by the Swedish Nuclear Fuel and Waste Management Co. This drilling technique preserves fragile minerals on fracture surfaces, facilitating the investigation of ancient biological activity in deep fracture systems. Barite was sampled from fractures in a total of 40 drill cores. The samples represented depths ranging from 60 to 1,660 m below sea level. The exact locations of the boreholes are provided in the Supplementary Dataset. Sample

characterization and mineral identification were performed directly on the fracture surfaces using a FEI QUANTA FEG 650 Scanning Electron Microscope (SEM) equipped with an integrated energy-dispersive spectroscopy (EDS, Oxford T-Max 80 detector) under low-vacuum conditions. The acceleration voltage was 20 kV, and the instrument was calibrated with a cobalt standard. The barite grains were hand-picked from the fracture surface under a microscope, embedded in several epoxy mounts (2.5 cm diameter), and polished to expose cross-sections of the grains. The polished grains were examined using SEM prior to SIMS analysis to detect growth zonation and avoid impurities and cracks.

2.2 Secondary-ion mass spectrometry (SIMS) analysis of barite ($\delta^{18}O$ and $\delta^{34}S$)

Secondary-ion mass spectrometry (SIMS) was conducted on a CAMECA IMS1280 ion probe at the NordSIMS lab, Swedish Museum of Natural History, Stockholm. The analytical routines for S and O isotope analyses of barite follow those described by Drake et al. (2024), which are based on the approaches by Whitehouse (2013) for S and Heinonen et al. (2015) for O. The samples were sputtered using a $^{133}Cs^+$ primary beam with 20 kV incident energy and a beam current of ~3 nA, which was rastered over a 5 × 5 μm area during analysis. Each analysis comprised 40 s of pre-sputtering to remove the gold coating over a 15 × 15 μm area, centering of the secondary beam in the field aperture, and data acquisition in 12 four-second integration cycles. Secondary ion signals (^{32}S and ^{34}S or ^{16}O and ^{18}O) were detected simultaneously using two Faraday detectors with a common mass resolution of 4,860 (M/ΔM) for S and 2,430 (M/ΔM) for O. Data were normalized for instrumental mass fractionation using the S0327 reference material, with a conventionally determined $\delta^{34}S$ value of +22.0±0.3 ‰ and $\delta^{18}O$ value of +11.0±0.1 ‰ (Liseroudi et al., 2021). All results are reported as $\delta^{34}S_{V\text{-}CDT}$ (Ding et al., 2001) for S and $\delta^{18}O_{V\text{-}SMOW}$ (Coplen, 1995) for O. The typical uncertainties after propagating the within-run and external uncertainties from the standard measurements were ±0.2 ‰ (1σ) for $\delta^{34}S$ and between ±0.2 and ±0.6 ‰ (1σ) for $\delta^{18}O$ values. The previously published calcite $\delta^{18}O_{V\text{-}PDB}$ values were converted to $\delta^{18}O_{V\text{-}SMOW}$ for comparability with barite using the formula $\delta^{18}O_{V\text{-}SMOW} = 1.03092 \times \delta^{18}O_{V\text{-}PDB} + 30.92$. All SIMS data, including previously published data, are compiled in the Supplementary Dataset.

2.3 Statistical analysis

Statistical analysis of 366 paired $\delta^{18}O_{barite}/\delta^{34}S_{barite}$ data was conducted using a Gaussian Mixture Model (GMM), which is a useful tool for classifying multivariate stable isotope data (Göhring et al., 2016). Notably, GMM is highly sensitive to outliers; hence, they need to be excluded before GMM to prevent adverse effects on the clustering performance. We identified outliers in the paired $\delta^{34}S$–$\delta^{18}O$ data using density-based spatial clustering of applications with noise (DBSCAN; Ester et al., 1996). DBSCAN identifies data points that do not belong to any dense region as noise without assuming a predetermined number or shape of clusters, making it useful for outlier detection in bivariate isotope datasets (Valentine et al., 2015). The parameters for DBSCAN are the minimum number of points (minPts) required to form a dense region and the neighborhood radius (ε). We tested the sensitivity of our outlier detection to these parameters over a range of minPts values (2 to 15). For each minPts value, ε was set at the point of maximum curvature of the sorted k-distance curve (k = minPts) (Ester et al., 1996) (Fig. S1).

The $\delta^{34}S$–$\delta^{18}O$ data were converted to z-scores before clustering to ensure neither variable dominated ε, and DBSCAN was run for each parameter pair (Fig. S2). The stability of the identified parameter combinations was quantified using the Jaccard index (the number of outliers identified in two neighboring minPts settings divided by the number identified in each), and the number of dense clusters was tracked across settings (Fig. S3). The number of clusters was stable at 2 for minPts ≥ 6, and neighboring minPts settings from 13 to 14 identified identical points as outliers (Jaccard = 1.00), indicating that DBSCAN using minPts values of 13 and 14 yields stable outlier detection results. Therefore, we used minPts = 13 and the associated ε = 0.586. This parameter combination identified 21 of 366 data points as outliers that were excluded before GMM.

We performed GMM on the outlier-cleaned data set using the Python module Scikit-learn (Pedregosa et al., 2011). To select the appropriate number of clusters for GMM in our $\delta^{18}O_{barite}/\delta^{34}S_{barite}$ dataset, we identified the best-fit model by calculating the Bayesian Information Criterion (BIC) as a function of the number of clusters. The minimum BIC value indicated our dataset contained two clusters (Fig. S4A). Random state optimization for GMM was performed over a range of zero to ten, yielding a random state of zero at the minimum BIC. York regression was used to calculate the slopes and r^2 values of the resulting clusters (Fig. S4B) (York et al., 2004). Notably, our dataset contains data points from two localities (i.e., Laxemar and Forsmark), whereas Laxemar provides the dominant fraction (323 vs. 21 for S). Deriving robust and meaningful clusters requires consistent behavior of these clusters across localities. Hence, we tested the sensitivity of our GMM approach to differences between localities by excluding Forsmark and repeating the same GMM procedure described for the entire dataset. After excluding the Forsmark data, the BIC-guided decision for a two-cluster model remained robust (Fig. S4C). Additionally, the resulting slopes of the individual clusters changed minimally after excluding Forsmark data (Figs. S4B, S4D). This suggests our clusters were independent of the localities. Thus, we used the cluster assignment and slopes resulting from GMM of the whole dataset to interpret our dataset. In concert, these observations strongly support a two-cluster GMM approach for classifying our $\delta^{18}O_{barite}/\delta^{34}S_{barite}$ dataset. Nevertheless, the resulting clusters should not be regarded as globally representative and may differ for barite from other areas.

3 Results and discussion

3.1 Pyrite-calcite-barite assemblages record ancient microbial sulfate reduction in the deep subsurface

Coupled $\delta^{34}S_{pyrite}$ and $\delta^{13}C_{calcite}$ signatures provide evidence of ancient organotrophic sulfate reduction (OSR) and sulfate-dependent anaerobic oxidation of methane (AOM) in deep subsurface fractures at Forsmark and Laxemar (Drake et al., 2013, 2015, 2018, 2021). The compiled data from Forsmark and Laxemar showed a $\delta^{34}S_{pyrite}$ range of −53.9 to +131.7 ‰, a $\delta^{18}O_{calcite}$ range of +10.5 to +28.1 ‰, and a $\delta^{13}C_{calcite}$ range of −93.1 to +36.5 ‰ (Drake et al., 2017, 2018) (Table 1, Figs. 2-3). A prominent role of thermochemical sulfate reduction (TSR) in these localities has been ruled out because of the large apparent $^{34}\varepsilon$ between plausible $\delta^{34}S_{sulfate}$ values of fracture fluids in these systems and pyrite (55 to 66 ‰: Drake et al., 2021). Moreover, TSR generally occurs at temperatures >100 °C (Machel, 2001), which is inconsistent with fluid inclusion homogenization temperatures and clumped isotope thermometry indicating formation temperatures <100 °C of coeval calcite (Drake et al.,

2018; Herlambang et al., 2023). Thus, the wide $\delta^{34}S_{pyrite}$ range (−53.9 to +131.7 ‰) was interpreted to reflect Rayleigh distillation during microbial sulfate reduction (MSR) in semi-closed fracture systems, producing ^{34}S-depleted sulfide and extremely ^{34}S-enriched sulfate (Drake et al., 2018). The overall ranges of $\delta^{18}O_{barite}$ (−0.9 to +19.7 ‰) and $\delta^{34}S_{barite}$ (+7.6 to +52.0 ‰) across both localities are consistent with MSR, which can produce ^{18}O- and ^{34}S-enrichment in the residual sulfate pool (Antler et al., 2013, 2014, 2015; Brunner et al., 2005; Drake et al., 2018; Han et al., 2025; Jørgensen et al., 2004; Rudnicki et al., 2001; Wortmann et al., 2007; Zaback et al., 1993). These observations strongly suggest MSR could be recorded in co-genetic barite from Forsmark and Laxemar.

The extremely high $\delta^{34}S_{pyrite}$ values at Forsmark and Laxemar imply the presence of an even more ^{34}S-enriched sulfate reservoir potentially archived in co-genetic barite. To detect this archive and investigate its relationship with OSR and AOM, we analyzed $\delta^{34}S_{barite}$ and $\delta^{18}O_{barite}$ in the same drill cores that were previously sampled for $\delta^{34}S_{pyrite}$ and $\delta^{18}O_{calcite}$, and $\delta^{13}C_{calcite}$ analysis (Drake et al., 2017, 2018) (Figs. 2,3; Table 1). The $\delta^{34}S_{sulfate}$ values of the paleo-fracture fluids are unknown and likely changed over time. However, the $\delta^{34}S_{sulfate}$ values of the current fracture fluids (+14 to +27 ‰: Drake et al., 2013) are similar to the median $\delta^{34}S_{barite}$ values at Forsmark (+26.6 ‰) and Laxemar (+18.3 ‰), suggesting dissolved sulfate in such fluids is a plausible source for barite. The total range of $\delta^{34}S_{barite}$ (+7.6 to +52.0 ‰) is consistent with processing of such fracture fluids by MSR under closed-system conditions (Paytan et al., 2002). However, this range is much narrower than that of $\delta^{34}S_{pyrite}$ (−53.9 to +131.7 ‰) across Forsmark and Laxemar (Figs. 2,3; Table 1). The ancient barite from Forsmark and Laxemar does not record the extreme ^{34}S-enrichment expected from the $\delta^{34}S_{pyrite}$ data. This agrees with barite that recently precipitated on drill core equipment within a deep borehole at Äspö (Fichtner et al., 2024), and carbonate-associated sulfate from the Forsmark and Laxemar drill cores (Fichtner et al., 2026). Therefore, a record of extremely ^{34}S-enriched sulfate in the deep subsurface remains undetected.

Table 1: Stable isotope data ($\delta^{34}S$, $\delta^{18}O$, $\delta^{13}C$) of fracture-hosted minerals (barite, pyrite, calcite) from Forsmark and Laxemar (Fennoscandian Shield, Sweden). Barite data were analyzed in this study. Calcite and pyrite data were obtained from Drake et al. (2017, 2018).

	$\delta^{34}S_{barite}$ (‰, V-CDT)	$\delta^{18}O_{barite}$ (‰, V-SMOW)	$\delta^{34}S_{pyrite}$ (‰, V-CDT)	$\delta^{13}C_{calcite}$ (‰, V-PDB)	$\delta^{18}O_{calcite}$ (‰, V-SMOW)
Forsmark					
n	25	22	793	585	603
Min	+16.5	−0.9	−42.4	−70.3	+13.4
Max	+36.8	+16.9	+65.8	+36.5	+30.9
Average	+28.0	+12.4	+13.8	−10.8	+18.8
Median	+26.6	+15.1	+13.2	−11.8	+18.8
SD	7.3	5.0	16.5	17.2	2.6
Laxemar					
n	480	350	874	621	487

Min	+7.6	+3.1	−53.9	−93.1	+10.5
Max	+52.0	+19.7	+131.7	+7.1	+28.1
Average	+19.5	+12.3	+32.3	−16.5	+20.3
Median	+18.3	+12.3	+23.3	−9.6	+21.0
SD	6.7	3.0	43.8	19.7	3.4

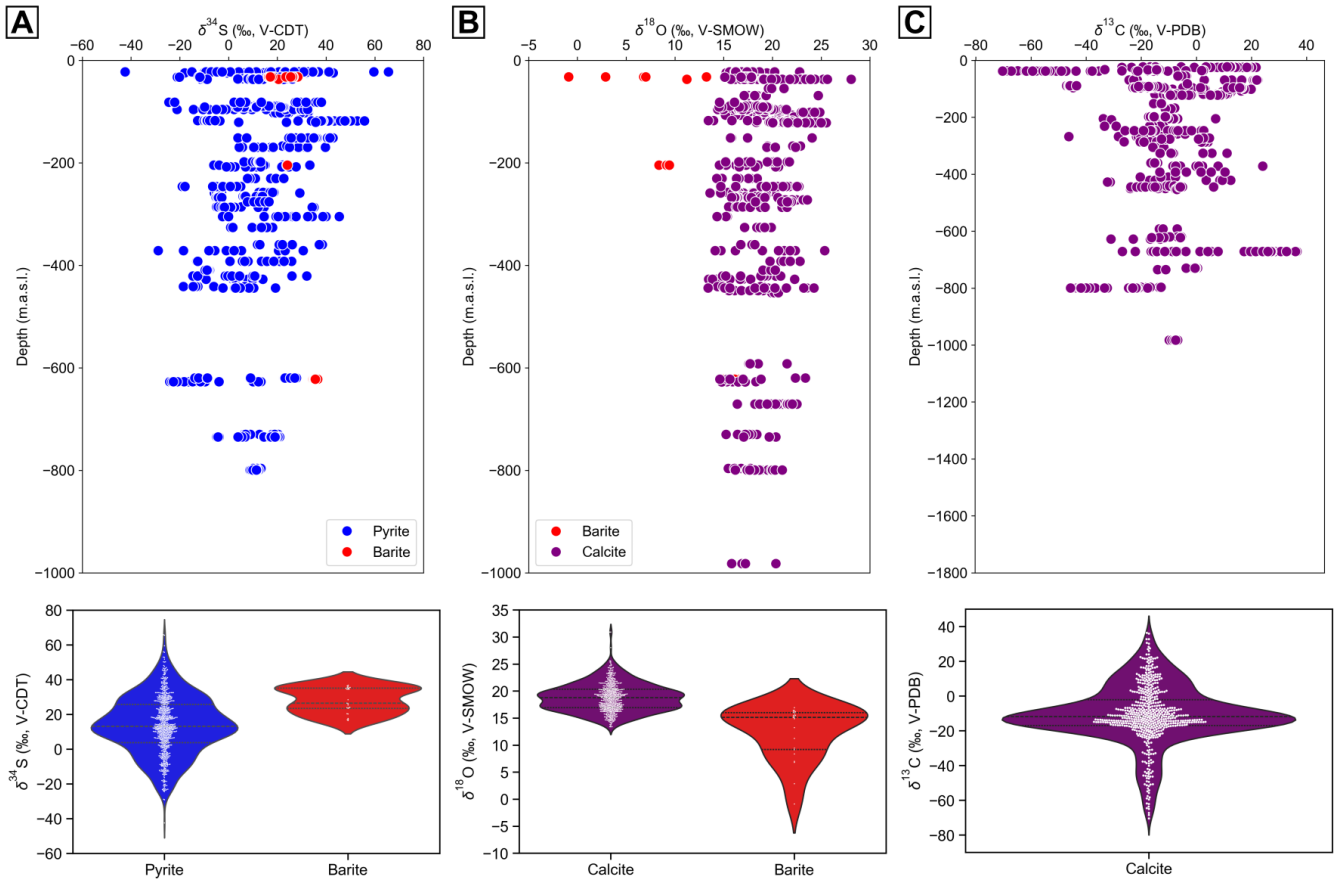


Figure 2: Depth distribution and violin plots of stable isotope data for fracture-hosted minerals from Forsmark. A: $\delta^{34}S_{barite}$, $\delta^{34}S_{pyrite}$. B: $\delta^{18}O_{barite}$, $\delta^{18}O_{calcite}$. The $\delta^{18}O_{calcite}$ data were converted from V-PDB to V-SMOW for comparison with $\delta^{18}O_{barite}$. C: $\delta^{13}C_{calcite}$. Each data point represents one SIMS analysis spot (m.a.s.l. = meters above sea level). Barite data were analyzed in this study. Calcite and pyrite were obtained from Drake et al. (2017, 2018).

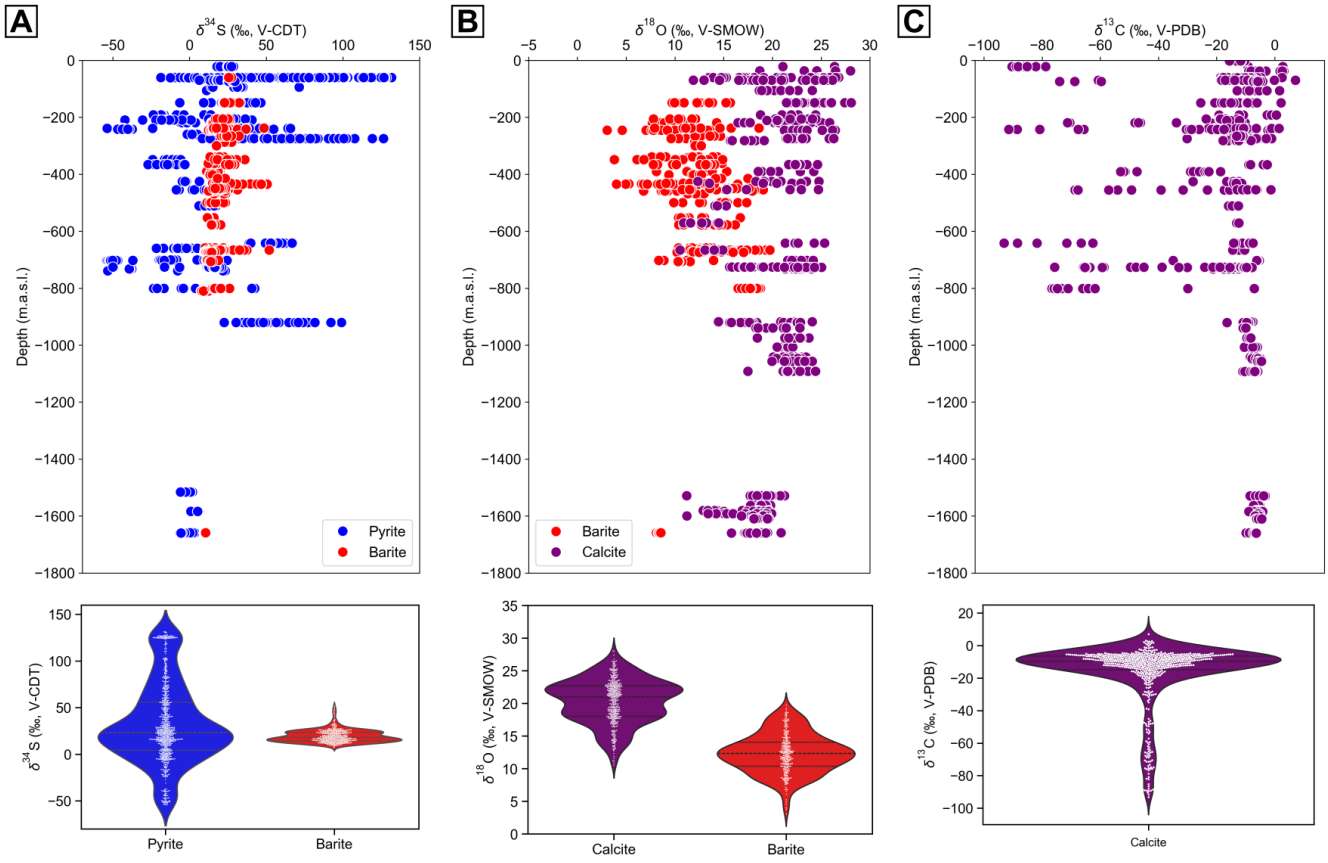


Figure 3: Depth distribution and violin plots of stable isotope data for fracture-hosted minerals from Laxemar. A: $\delta^{34}S_{barite}$, $\delta^{34}S_{pyrite}$. B: $\delta^{18}O_{barite}$, $\delta^{18}O_{calcite}$. The $\delta^{18}O_{calcite}$ data were converted from V-PDB to V-SMOW for comparison with $\delta^{18}O_{barite}$. C: $\delta^{13}C_{calcite}$. Each data point represents one SIMS analysis spot (m.a.s.l. = meters above sea level). Barite data were analyzed in this study. Calcite and pyrite were obtained from Drake et al. (2017, 2018).

3.2 Variable sulfate reduction rates and pathways explain microscale $\delta^{18}O$-$\delta^{34}S$-$\delta^{13}C$ data

The co-variation of the $\delta^{18}O_{barite}$ and $\delta^{34}S_{barite}$ values exhibited substantial scatter (Fig. 4A), implying a mixture of different sulfate sources and/or an overlap of different fractionation processes. Since the $\delta^{18}O/\delta^{34}S$ systematics of dissolved sulfate in the low-temperature groundwater systems at Forsmark and Laxemar are affected by OSR and AOM (Drake et al., 2017, 2018; Fichtner et al., 2024), we aimed to identify whether our dataset contains groups of barite associated with either OSR or AOM. To identify barite associated with these groups, we classified our dataset using Gaussian Mixture Modeling (GMM) and compared the linear regression slopes of the resulting clusters with known sulfate $\delta^{18}O/\delta^{34}S$ trends in MSR-affected settings. We identified a steeper trending 'Group 1' cluster (slope: 0.95 ± 0.01; r^2 = 0.39) and a shallower trending 'Group 2' cluster (slope: 0.55 ± 0.01; r^2 = 0.38) (Fig. 4A; Table 2). The clusters resulting from GMM are statistical entities and cannot be interpreted as continuous fractionation trends in our study. This is because our dataset contains multiple barite growth generations from different locations and records different fractionation trends, non-coeval sulfate reservoirs between growth

zones, or local fluid mixing. Therefore, our statistical analysis can only detect average $\delta^{18}O/\delta^{34}S$ trends of overlapping fractionation or mixing processes involving fracture water sulfate that was processed by OSR and AOM at different points in space and time. These overlapping trends likely explain the low r^2 values. There was no correlation between Group 1 or Group 2 barite and the $\delta^{18}O$ values of co-genetic calcite (Fig. 4B). This suggests that the difference between Group 1 and Group 2 does not simply reflect isotopically distinct water sources (Pedersen et al., 1997). Instead, they most likely record different processes affecting the respective sulfate reservoirs from which barite precipitated.

Previous studies established that sulfate reduction rates (SRR) control the $\delta^{18}O/\delta^{34}S$ slope in residual sulfate during the early stages of MSR (Brunner et al., 2005; Han et al., 2025; Wortmann et al., 2007). At a lower SRR, $\delta^{18}O$ rises rapidly relative to $\delta^{34}S$ leading to a steeper slope, whereas at a higher SRR, $\delta^{18}O$ rises slowly relative to $\delta^{34}S$, leading to a shallower slope (Fig. 1). Thus, the difference in $\delta^{18}O/\delta^{34}S$ slopes could reflect a lower SRR in Group 1 than in Group 2 barite (Fig. 4A). Moreover, differences in metabolic pathways (OSR vs. AOM) can lead to variable $\delta^{18}O/\delta^{34}S$ trends in sulfate at similar SRR (Antler et al., 2013, 2014, 2015). To clarify the effects of SRR and MSR pathways on $\delta^{18}O/\delta^{34}S$ systematics recorded in barite at Forsmark and Laxemar, we correlated our GMM-classified $\delta^{18}O_{barite}$ and $\delta^{34}S_{barite}$ data (i.e., excluding outliers) with the $\delta^{13}C$ values of calcite in the same samples (Figs. 2C,3C,4C). When petrographic correlation of barite with individual calcite generations was not possible, we used average $\delta^{13}C_{calcite}$ values from the barite-bearing samples. Out of all classified barite data, 71 spots in Group 1 and 81 spots in Group 2 had associated $\delta^{13}C_{calcite}$ data. Strongly ^{13}C-depleted calcite ($\delta^{13}C < -40$ ‰) was almost exclusively associated with Group 1 barite (28 out of 71) (Fig. 4C). The $\delta^{13}C$ values of this calcite (−70 to −40 ‰) cannot be explained by oxidation of organic matter via OSR alone and suggest variable input of inorganic C from the oxidation of primarily microbial methane (Drake et al., 2015, 2017). This implies that some Group 1 barite associated with such calcite was affected by AOM. In contrast, only 2 out of 81 spots in Group 2 barite were associated with strongly ^{13}C-depleted calcite. Instead, Group 2 was almost exclusively associated with calcite that has a $\delta^{13}C \approx -30$ ‰ or higher (Fig. 4C), suggesting methane was not the main C source (Whiticar, 1999). This calcite likely reflects a more prominent contribution from organic matter rather than methane oxidation, implying that the associated barite was affected by OSR (Drake et al., 2017). Notably, such OSR-related barite not only dominates Group 2, but also widely occurs in the AOM-affected Group 1 (Fig. 4C). Thus, it seems unlikely that the different MSR pathways are the only control on the different slopes of both groups. Instead, we interpret the different $\delta^{18}O/\delta^{34}S$ trends to result from an interplay of MSR pathways and SRR: Group 1 reflects AOM and OSR at a relatively low SRR, whereas Group 2 dominantly reflects OSR at a relatively high SRR.

The outliers identified via DBSCAN (n = 21) are strongly heterogeneous and do not follow a common $\delta^{18}O/\delta^{34}S$ trend (Fig. 4A, Table 2). Thus, the outliers do not form a coherent group and likely reflect highly variable fluid compositions and fractionation processes. Moreover, a relationship of the outliers with fluid sources and MSR pathways is unclear because only four outliers have associated $\delta^{18}O_{calcite}$ and $\delta^{13}C_{calcite}$ values (Fig. 4B, C).

Table 2: Statistical parameters of the groups resulting from the Gaussian Mixture Model.

	Min	Max	Median	Average	SD

Group 1 (n=221)					
$\delta^{34}S_{barite}$ (‰, V-CDT)	+9.4	+25.2	+15.1	+15.2	3.1
$\delta^{18}O_{barite}$ (‰, V-SMOW)	+6.8	+19.1	+12.7	+12.8	2.9
Group 2 (n=124)					
$\delta^{34}S_{barite}$ (‰, V-CDT)	+15.5	+36.8	+24.3	+25.0	5.0
$\delta^{18}O_{barite}$ (‰, V-SMOW)	+5.3	+18.6	+11.6	+11.6	2.6
Outliers (n=21)					
$\delta^{34}S_{barite}$ (‰, V-CDT)	+12.1	+52.0	+35.5	+34.5	12.1
$\delta^{18}O_{barite}$ (‰, V-SMOW)	−0.9	+19.7	+11.8	+11.1	6.4

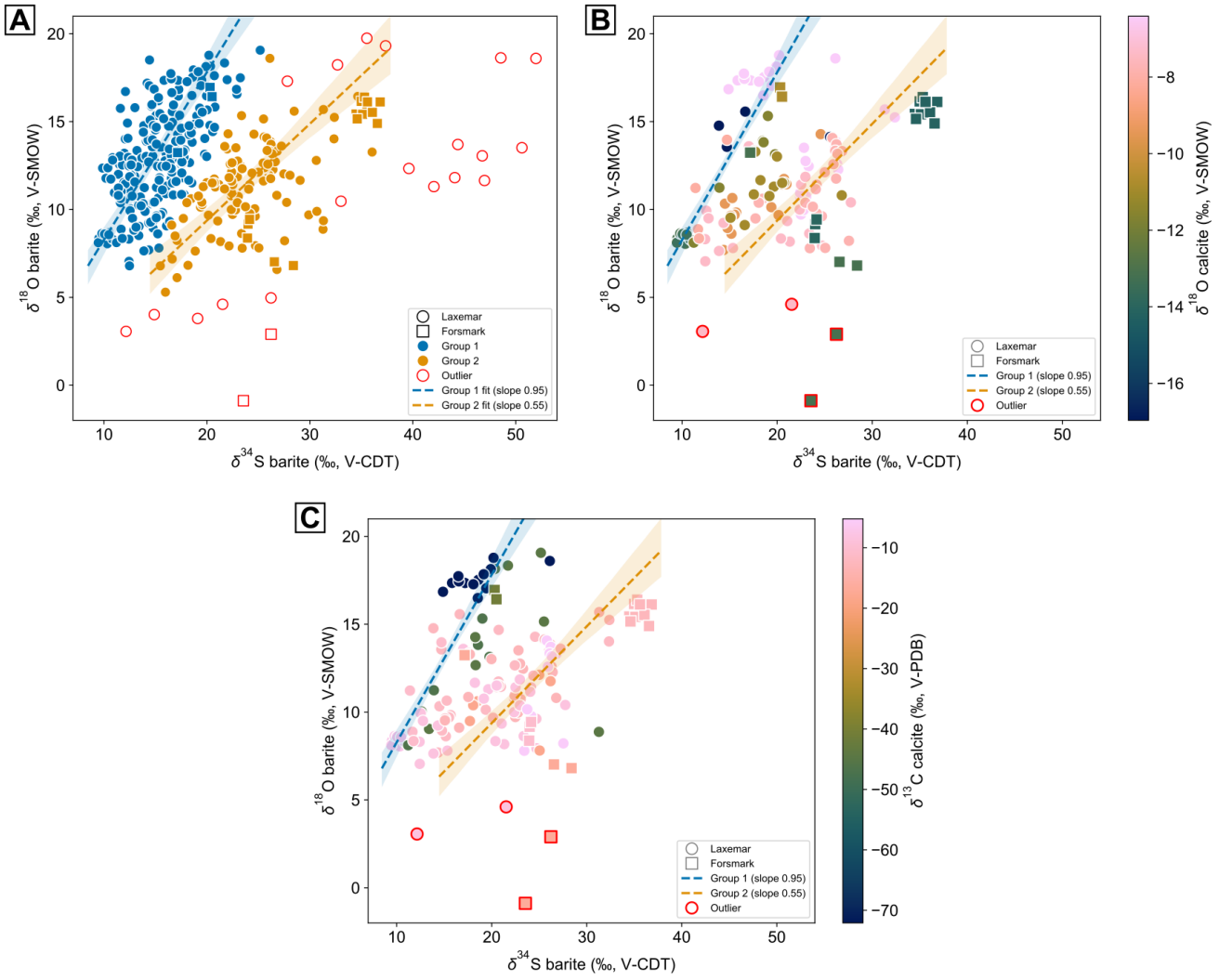


Figure 4: Gaussian Mixture Modeling (GMM) of barite $\delta^{18}O$-$\delta^{34}S$ data and correlation with published calcite $\delta^{18}O$-$\delta^{13}C$ data. Each data point represents one spot with paired SIMS $\delta^{18}O$ and $\delta^{34}S$ analyses. A: $\delta^{18}O$ and $\delta^{34}S$ analyses of barite and GMM-derived cluster assignments of data points. The two-component GMM of barite $\delta^{18}O$ and $\delta^{34}S$ data after exclusion of outliers (black) yielded 'Group 1' and 'Group 2' barite. York regression yielded slopes of 0.95 for Group 1 and 0.55 for Group 2. The ranges of the regression lines equal the data range used for GMM and cannot be extended to the outliers. B: $\delta^{18}O$ and $\delta^{34}S$ analyses of barite color-coded by $\delta^{18}O$ of calcite in the same sample. There was no apparent correlation between the Group 1 and Group 2 trends and their corresponding $\delta^{18}O_{calcite}$ values, demonstrating that the trends arise from fractionation processes affecting the sulfate reservoir, rather than fluid mixing. C: $\delta^{18}O$ and $\delta^{34}S$ analyses of barite color-coded by $\delta^{13}C_{calcite}$ in the same sample. The $\delta^{13}C_{calcite}$ data suggest that AOM barite occurs almost exclusively in Group 1. In contrast, OSR-related barite occurred in Groups 1 and 2. The color coding in B & C follows recommendations for scientifically derived color maps (Crameri et al., 2020).

3.3 Hydrogeochemical controls on sulfate reduction rates and pathways

The major control on SRR is the availability and quality of electron donors (i.e., H_2, CH_4, or organic matter) (Leavitt et al., 2013; Lyons and Gaudette, 1979; Westrich and Berner, 1984). SRR is high when electron donors are more bioavailable and

abundant, and vice versa. The abundances of electron donors in the parent fluids from which our ancient barite precipitated are unknown. However, low SRR due to nutrient limitation was inferred based on the large apparent $^{34}\varepsilon$ associated with pyrite formation at these sites (Drake et al., 2018), consistent with the common free energy limitation in deep subsurface habitats in general (Hoehler and Jørgensen, 2013). Thus, a relatively lower availability of electron donors in Group 1 could have caused the lower inferred SRR than in Group 2 (Fig. 5A). Moreover, the typical range of sulfate concentrations in modern anoxic fracture fluids at Forsmark and Laxemar (<1 to 10 mM: Hallbeck & Pedersen, 2008; Laaksoharju et al., 2008; Drake et al., 2013) is much lower than in marine environments (28 mM in seawater: Jørgensen et al., 2019). Such sulfate concentrations may additionally limit SRR in the deep subsurface (Boudreau and Westrich, 1984; Pallud and Van Cappellen, 2006). Sulfate concentrations in these subsurface habitats also vary around the threshold at which sulfate reducers outcompete methanogens for substrate utilization (ca. 1-10 mM: Iversen & Jorgensen, 1985; Glossner et al., 2016; Sela-Adler et al., 2017). If sulfate concentrations exceed this threshold, OSR can be favored, inhibiting methanogenesis and AOM. Thus, $\delta^{13}C$ evidence for AOM indirectly supports sulfate limitation in Group 1 (Fig. 4c). Thus, a combined effect of electron donor limitation and low sulfate concentrations could have favored methanogenesis and AOM at relatively low SRR (Fig. 5A). Conversely, a higher abundance of electron donors could explain a higher inferred SRR in Group 2 than in Group 1 (Fig. 5B). At higher sulfate availability, methanogenesis is inhibited, possibly resulting in a lack of evidence for AOM in Group 2 (Fig. 5B). Instead, OSR is favored and SRR is high, resulting in a shallower trend in Group 2 (Fig. 5B). Thus, we interpret the relative abundances of sulfate and electron donors to control the observed $\delta^{18}O/\delta^{34}S$ trends in ancient subsurface barite by modulating SRR and MSR pathways. The stronger ^{34}S-enrichment in the OSR-dominated Group 2 than in the AOM-affected Group 1 contrasts with observations from marine sediments, where ^{34}S-enriched barite is a commonly used proxy for AOM at the SMTZ (Torres et al., 1996; Wood et al., 2021; Yang et al., 2023; Zan et al., 2022; Zhou et al., 2015). This discrepancy could be due to the higher sulfate concentration in seawater (28 mM: Jørgensen et al., 2019) compared to the subsurface at Forsmark and Laxemar (<1 to 10 mM), allowing sulfate to become strongly ^{34}S-enriched before barite becomes undersaturated (Fichtner et al., 2024). The relatively steep slope of the AOM-affected Group 1 is comparable to some previous observations from marine methane-diffusion-limited AOM settings, such as sedimentary SMTZs, or OSR-dominated methane-devoid settings (Antler et al., 2013, 2015; Blake et al., 2006; Böttcher et al., 2006). At the same time, Group 2 shows little clear evidence of AOM but a shallow slope similar to marine methane-in-excess environments (i.e., the methane flux exceeds methane consumption via oxidation), such as cold seeps (Aharon and Fu, 2000, 2003; Antler et al., 2013, 2014; Rubin-Blum et al., 2014). These observations highlight a further discrepancy between marine environments and the deep subsurface. In marine environments, steeper $\delta^{18}O/\delta^{34}S$ slopes tend to be found in settings affected by OSR or methane-limited AOM, whereas shallower slopes result from AOM at high methane concentrations. In our subsurface barite, steeper slopes tend to be more associated with evidence for AOM, whereas shallower slopes tend to occur in OSR-dominated settings. The relatively shallow slope of OSR-related barite in the subsurface implies a lesser extent of equilibrium isotope exchange of S intermediates with water compared to marine settings. This could be achieved via a higher overall SRR in the subsurface than in marine settings; however, this seems unlikely given the oligotrophic nature of subsurface habitats (Küsel and Dopson, 2026). Additional factors influencing the

different behavior of $\delta^{18}O/\delta^{34}S$ trends in the deep subsurface may be the increasing temperature and pressure with depth or factors within microbial communities, such as low cell densities or adaptations to extreme nutrient limitation. However, the impact of these factors on $\delta^{18}O/\delta^{34}S$ relationships in residual sulfate during MSR remains speculative. Irrespective of this unresolved problem, the differences in $\delta^{18}O/\delta^{34}S$ systematics between marine and subsurface barite highlight that interpretations cannot be extended from one system to the other without additional constraints.

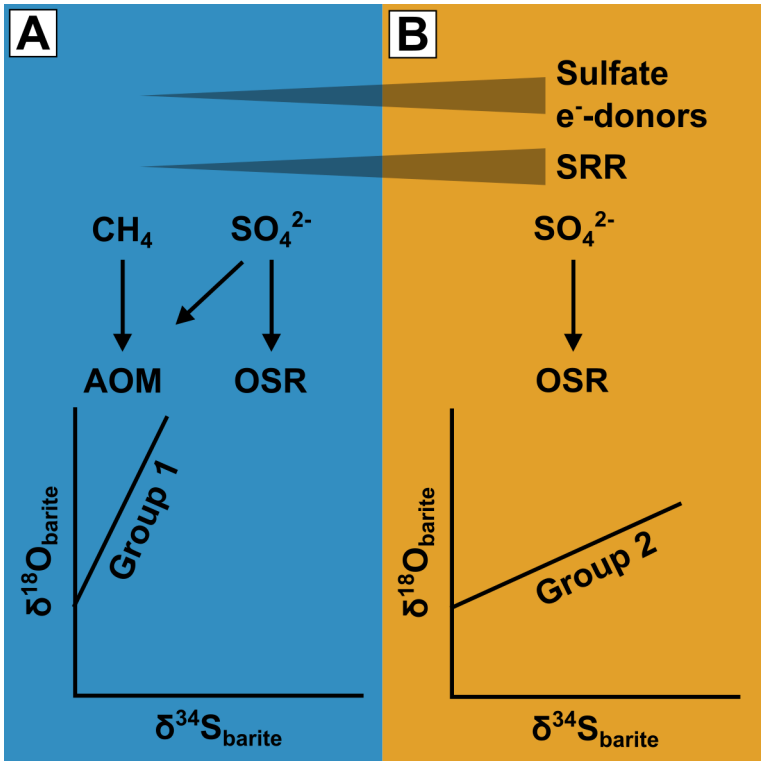


Figure 5: Conceptual model of the controls on $\delta^{18}O_{barite}$ and $\delta^{34}S_{barite}$ systematics in the continental deep subsurface. A: At low sulfate and electron donor abundances, microbial methanogenesis occurs and microbial sulfate reduction proceeds via both sulfate-dependent anaerobic oxidation of methane (AOM) and organotrophic sulfate reduction (OSR) at a relatively low sulfate reduction rate (SRR). This results in the steep $\delta^{18}O_{barite}/\ \delta^{34}S_{barite}$ trend recorded in Group 1 barite. B: At higher sulfate and electron donor abundance, microbial methanogenesis is inhibited, and MSR proceeds predominantly via OSR at relatively high SRR. This results in the shallow $\delta^{18}O_{barite}/\ \delta^{34}S_{barite}$ trend recorded in Group 2.

3.4 Barite and pyrite record distinct hydrogeochemical regimes

The absence of extreme ^{34}S-enrichment in barite from Forsmark and Laxemar is unexpected considering the corresponding $\delta^{34}S_{pyrite}$ values of up to +131.7 ‰, predicting an even more ^{34}S-enriched sulfate reservoir during pyrite formation. The $\delta^{34}S_{barite}$ values of up to +52.0 ‰ observed among the outliers suggest that the SRR at times exceeded the sulfate resupply, decreasing the steady-state sulfate concentration (i.e., closed-system conditions) (Fig. 4A). Hence, Rayleigh distillation is locally recorded in subsurface barite, although not to the extreme degree observed in pyrite (Table 1). This discrepancy between the barite and pyrite records has been suggested to result from (i) the precipitation of barite and pyrite under separate microenvironmental

conditions, involving the isolation of evolved ^{34}S-enriched fluids, or (ii) late-stage barite undersaturation which may inhibit sulfate precipitation or favor its post-formation dissolution before the formation of a ^{34}S-enriched sulfate reservoir (Fichtner et al., 2024, 2026). Barite undersaturation may arise from sulfate depletion at high degrees of Rayleigh distillation (Fichtner et al., 2024; Wood et al., 2021). Alternatively, barite precipitation during earlier stages may deplete Ba^{2+} (Aloisi et al., 2004), which in crystalline bedrock fractures is mainly supplied by feldspar dissolution. However, none of the $\delta^{34}S$ analyses of carbonate-associated sulfate in the samples analyzed here detected this reservoir (Fichtner et al., 2026). This suggests that the mechanism limiting the precipitation of extremely ^{34}S-enriched sulfate is more likely associated with the S cycle, rather than cation availability. Sampling biases cannot be excluded but have been mitigated by the large number of $\delta^{34}S$ analyses (n = 505) of barite from multiple fractures at two localities. Notably, the strongest ^{34}S-enrichment observed here occurs in the outlier group and is not associated with cogenetic calcite data (Fig. 4A-C; Table 2). This makes an interpretation of the associated MSR pathway and SRR difficult for these cases. However, it seems likely that these barites represent relatively late-stage precipitates that possibly formed in an environment where barite saturation was less limiting.

Microscale observations of pyrite-calcite-barite assemblages could help investigate this interpretation further (Figs. 6,7). Sample KAS02 (802 m) can serve as an example of AOM-associated barite due to its association with calcite that has an average $\delta^{13}C$ of −72.1 ‰ and pyrite with $\delta^{34}S$ values spanning −23.5 to +42.5 ‰ (Fig. 6A, B). Additionally, all SIMS spots on barite in this sample belong to Group 1 (Fig. 7A). Together, these observations are consistent with a sulfate pool affected by AOM at relatively low SRR. Notably, this barite exhibited distinct crystallographic and isotopic zonation with only minor $\delta^{34}S$ and $\delta^{18}O$ variabilities between growth zones of ~4 and ~0.8 ‰, respectively (Fig. 7B). This low variability suggests relatively open system conditions during barite growth (Fichtner et al., 2024; Wood et al., 2021). In contrast, the much more pronounced core-to-rim $\delta^{34}S$ increase in the co-genetic pyrite from −23.5 to +42.5 ‰ indicates MSR in a more closed system, meaning that SRR exceeded the resupply of sulfate during pyrite growth (Fig. 7C). Apparently, barite and pyrite in this sample record precipitation in distinct hydrogeochemical regimes, possibly at different stages of fracture fluid evolution or in separate microenvironments.

Sample KLX01 (220 m) serves as an example of OSR-related barite due to its association with calcite lacking a substantial $\delta^{13}C$ depletion (−11.6 ‰) (Fig. 6C, D). Notably, barite in this sample exhibited a massive core and a porous rim (Fig. 7D). These texturally distinct growth zones were associated with a sharp core-to-rim $\delta^{34}S$ and $\delta^{18}O$ increase of ~12 ‰ and ~6 ‰, respectively (Fig. 7D,E). This sharp increase suggests that barite in the rim precipitated from sulfate that had already undergone ^{34}S-enrichment via sulfate reduction elsewhere in the fracture system (e.g., Drake et al., 2018). Additionally, SIMS spots related to Group 1 predominated in the core, whereas spots related to Group 2 exclusively occurred in the rim (Fig. 7D). This implies that the processing of the respective sulfate reservoirs reflected by core and rim occurred under different SRR and/or MSR pathways. Thus, the distinct textural and isotopic differences demonstrate that the generations reflect two barite precipitation events, rather than continuous barite growth. The porosity in the rim suggests barite dissolution (Fig. 7D), possibly due to undersaturation via rapid sulfate depletion at the high SRR inferred for Group 2 (Fichtner et al., 2024). Thus, a relatively high SRR in a sulfate-poor environment may result in a preservation bias against extremely ^{34}S-enriched barite in

deep subsurface environments. The relatively minor core-to-rim $\delta^{34}S$ increase of ca. 0 to 20 ‰ in co-genetic pyrite implies that sulfate did not become strongly depleted during pyrite formation in this microenvironment (Fig. 7F). While there was no evidence for AOM from $\delta^{13}C_{calcite}$ in this sample, it cannot be resolved petrographically whether the calcite and pyrite are co-genetic to the barite core or rim. Therefore, it remains unclear whether the shift from Group 1 to Group 2 during barite growth is due to different MSR pathways or SRR, or both. Nevertheless, the differences between the samples KAS02 (802 m) and KLX01 (220 m), as well as their evolution during barite growth, demonstrate a strong control of hydrogeochemical conditions on their isotopic composition in different microenvironments and over time. This highlights that the associated barite and pyrite record different environmental conditions and should be correlated with caution.

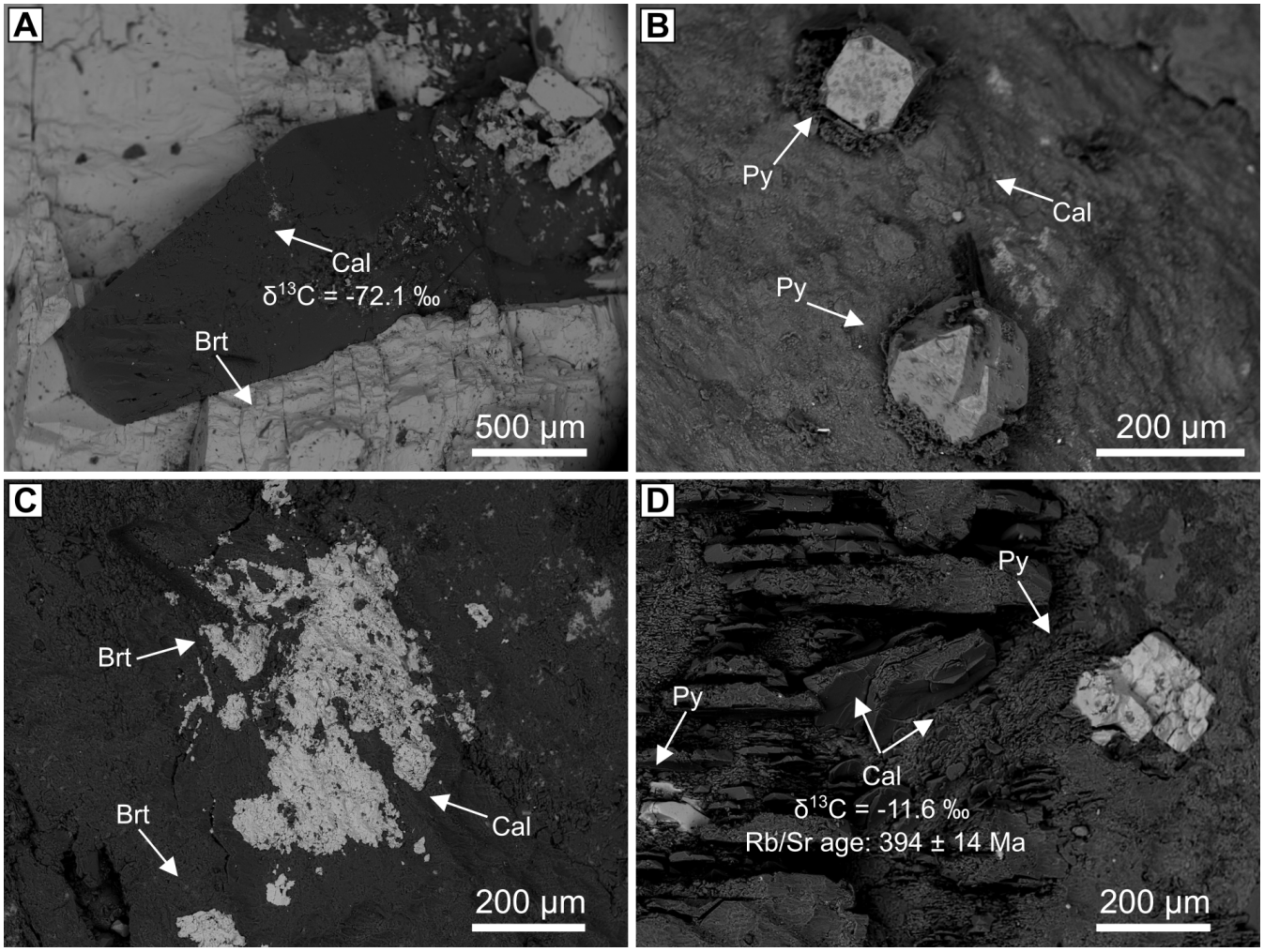


Figure 6: Backscatter electron micrographs of calcite-pyrite-barite assemblages in drill core samples investigated in this study. A-B: Sample KAS02 (802 m depth) from Äspö (i.e., Laxemar). A: Barite (Brt) intergrown with calcite (Cal), demonstrating the coeval formation of barite and calcite. Calcite in this sample has an average $\delta^{13}C$ of −72.1‰, demonstrating calcite precipitation after the oxidation of biogenic methane via AOM (Drake et al., 2017). B: Euhedral pyrite (Py) intergrown with calcite, demonstrating that pyrite is co-genetic with the outermost calcite generation. C-D: Sample KLX01 (220 m depth) from Laxemar. C: Barite intergrown with calcite, demonstrating their co-genetic relationship. D: Pyrite intergrown with calcite, demonstrating the coeval formation of

pyrite with calcite and, thus, barite. The calcite generation coeval with barite has a Rb/Sr age of 394 ± 14 Ma and $\delta^{13}C_{calcite}$ = −11.6 ‰ (Drake et al., 2017).

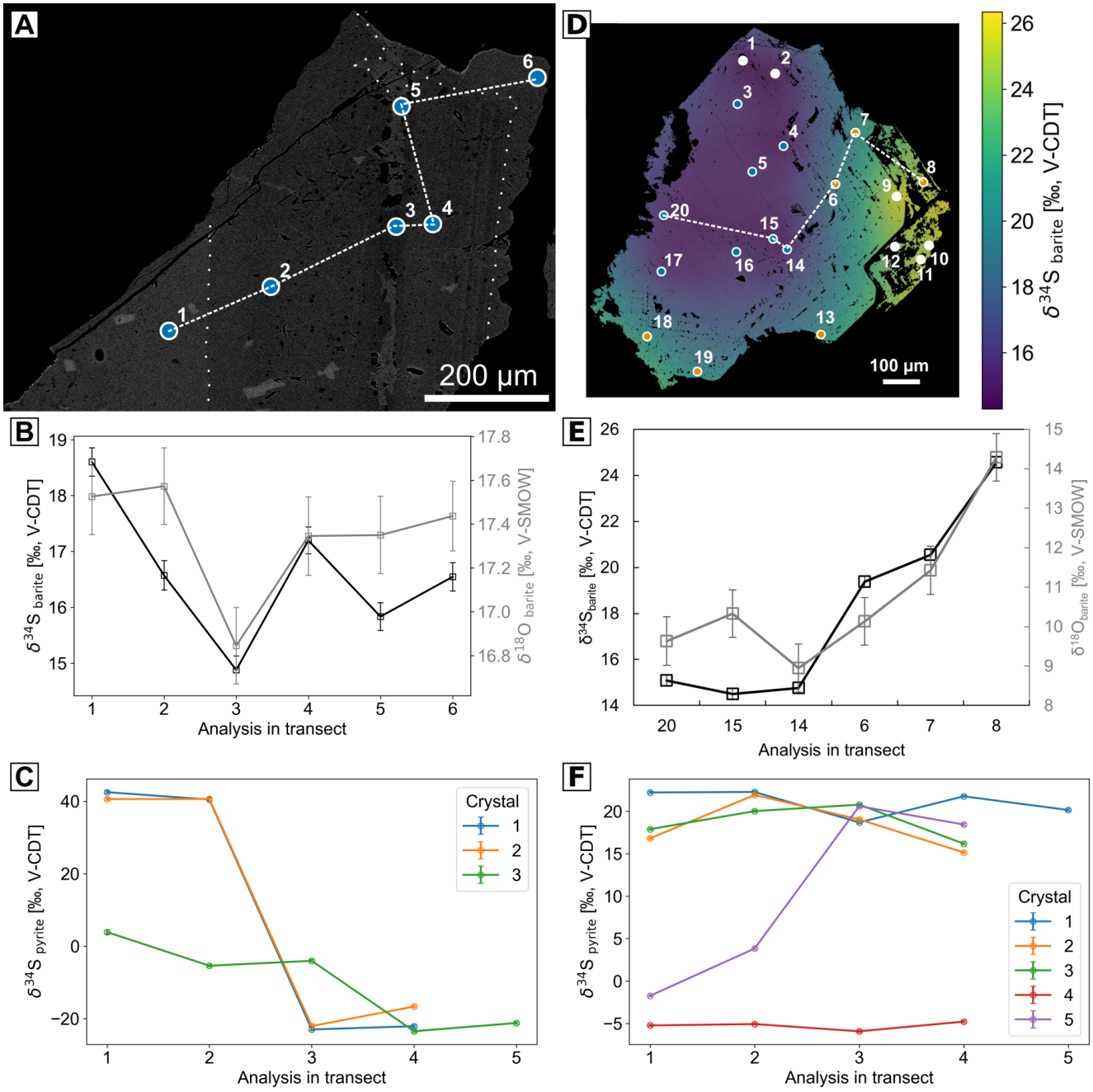


Figure 7: Microscale stable isotope variations in individual barite and pyrite grains. A: SEM image of a polished barite grain with three distinct growth zones in sample KAS02 (802 m depth) from Äspö (i.e., Laxemar). The white dotted lines highlight the boundaries between growth zones, whereas the white dashed lines highlight analytical transects. B-C: SIMS analytical transects of barite and associated pyrite in the same sample (A). Transects across three pyrite crystals from the same sample show a $\delta^{34}S_{pyrite}$

variation of ca. 65 ‰ across two of the crystals. D: SEM image of a polished barite grain with two distinct growth zones and SIMS analytical transects of barite and associated pyrite in sample KLX01 (220 m depth) from Laxemar. The overlain heatmap was interpolated via cubic convolution and does not reflect measured $\delta^{34}S$ values beyond the analyzed spots. E-F: SIMS analytical transects of barite and associated pyrite in the same sample (D). The transect across a zoned barite crystal (E) shows co-variation of $\delta^{34}S_{barite}$ and $\delta^{18}O_{barite}$ with higher ^{34}S- and ^{18}O-enriched values in the later generation (rim). The transect across five pyrite grains shows a $\delta^{34}S_{pyrite}$ variation of ca. 20 ‰ across one grain (F). The color coding of the analysis spots in (A) and (D) reflects their assignment to Group 1 (blue) and Group 2 (orange) according to Fig. 4A. White dots could not be assigned to a group because corresponding $\delta^{18}O_{barite}$ values were lacking. The error bars associated with pyrite analyses are smaller than the symbols.

4 Conclusions

We compiled previously published microscale $\delta^{13}C_{calcite}$, $\delta^{18}O_{calcite}$, and $\delta^{34}S_{pyrite}$ data with new SIMS $\delta^{18}O_{barite}$ and $\delta^{34}S_{barite}$ analyses to investigate biosignature records in ancient deep subsurface mineral assemblages from Forsmark and Laxemar/Äspö (Southeastern Sweden). We identified two groups of barites recording microbial sulfate reduction (MSR) associated with distinct $\delta^{18}O/\delta^{34}S$ slopes. Comparison with coeval $\delta^{13}C_{calcite}$ data revealed that evidence for sulfate-dependent anaerobic oxidation of methane (AOM) is mostly restricted to the steeper-trending Group 1, whereas Group 2 was dominated by organotrophic sulfate reduction (OSR). We interpret the different slopes to result from an interplay of variable sulfate reduction rates (SRR) and MSR pathways (AOM vs. OSR): Group 1 reflects AOM and OSR at relatively low SRR, whereas Group 2 dominantly reflects OSR at relatively high SRR. Variations in SRR and MSR pathways likely reflect the relative sulfate and electron donor abundances in the barite's parent fluids. Barite records $\delta^{34}S$ values up to +52.0 ‰, which is well below the extreme ^{34}S-enrichment observed in some pyrite from the same locality ($\delta^{34}S_{pyrite}$ = +131.7 ‰). The discrepancy between barite and pyrite records could reflect their formation in separate microenvironments or may be due to undersaturation caused by sulfate and/or Ba^{2+} depletion at high degrees of Rayleigh distillation. In concert, microscale C-O-S isotope signatures in fracture-hosted pyrite-calcite-barite assemblages at Forsmark and Laxemar record biosignatures of AOM and OSR deep within the Fennoscandian Shield since at least 394 Ma, but these records are affected by local hydrogeochemical conditions. Signatures of metabolic processes in barite varied over time within the same microenvironment and between different fractures. This highlights that understanding deep subsurface geobiology requires integrated microscale analyses of mineral assemblages distributed over large crustal volumes.

Data availability

All data presented in the manuscript are available in the Supplementary Dataset via the online repository Zenodo (doi:10.5281/zenodo.22041131).

Author contributions

ER: Data curation, Formal analysis, Investigation, Methodology, Validation, Visualization, Writing (original draft preparation), Writing (review and editing). VF: Data curation, Investigation, Formal analysis, Writing (review and editing).

MT: Data curation, Investigation, Formal analysis, Writing (review and editing). MW: Resources, Writing (review and editing). HD: Conceptualization, Funding acquisition, Methodology, Project administration, Resources, Supervision, Writing (review and editing).

Competing interests

The authors declare no competing interests.

Acknowledgements

This work was supported by grants of the Swedish Nuclear Fuel and Waste Management Co. (SKB), Swedish Research Council (2021-04365, 2025-04466), Formas (2020-01577), J. Gust. Richert foundation (2023-00850), the Crafoord foundation (20210524), and the National Science Foundation (2120733) to Henrik Drake. We thank Heejin Jeon for assistance in SIMS sample preparation and analysis and Andrea Göhring for valuable input on our statistical methodology. The AI tool Claude (Anthropic PBC) was used to help generate code for statistical analysis, and all generated output has been verified by the authors. This is NordSIMS publication #XXX.

References

Aharon, P. and Fu, B.: Microbial sulfate reduction rates and sulfur and oxygen isotope fractionations at oil and gas seeps in deepwater Gulf of Mexico, Geochimica et Cosmochimica Acta, 64, 233–246, https://doi.org/10.1016/S0016-7037(99)00292-6, 2000.

Aharon, P. and Fu, B.: Sulfur and oxygen isotopes of coeval sulfate–sulfide in pore fluids of cold seep sediments with sharp redox gradients, Chemical Geology, 195, 201–218, https://doi.org/10.1016/S0009-2541(02)00395-9, 2003.

Aloisi, G., Bouloubassi, I., Heijs, S. K., Pancost, R. D., Pierre, C., Sinninghe Damsté, J. S., Gottschal, J. C., Forney, L. J., and Rouchy, J.-M.: CH4 -consuming microorganisms and the formation of carbonate crusts at cold seeps, Earth and Planetary Science Letters, 203, 195–203, https://doi.org/10.1016/S0012-821X(02)00878-6, 2002.

Aloisi, G., Wallmann, K., Bollwerk, S. M., Derkachev, A., Bohrmann, G., and Suess, E.: The effect of dissolved barium on biogeochemical processes at cold seeps, Geochimica et Cosmochimica Acta, 68, 1735–1748, https://doi.org/10.1016/j.gca.2003.10.010, 2004.

Anderson, T. F., Kruger, J., and Raiswell, R.: C-S-Fe relationships and the isotopic composition of pyrite in the New Albany Shale of the Illinois Basin, U.S.A., Geochimica et Cosmochimica Acta, 51, 2795–2805, https://doi.org/10.1016/0016-7037(87)90159-1, 1987.

Antler, G., Turchyn, A. V., Rennie, V., Herut, B., and Sivan, O.: Coupled sulfur and oxygen isotope insight into bacterial sulfate reduction in the natural environment, Geochimica et Cosmochimica Acta, 118, 98–117, https://doi.org/10.1016/j.gca.2013.05.005, 2013.

Antler, G., Turchyn, A. V., Herut, B., Davies, A., Rennie, V. C. F., and Sivan, O.: Sulfur and oxygen isotope tracing of sulfate driven anaerobic methane oxidation in estuarine sediments, Estuarine, Coastal and Shelf Science, 142, 4–11, https://doi.org/10.1016/j.ecss.2014.03.001, 2014.

Antler, G., Turchyn, A. V., Herut, B., and Sivan, O.: A unique isotopic fingerprint of sulfate-driven anaerobic oxidation of methane, Geology, 43, 619–622, https://doi.org/10.1130/G36688.1, 2015.

Bar-On, Y. M., Phillips, R., and Milo, R.: The biomass distribution on Earth, Proc. Natl. Acad. Sci. U.S.A., 115, 6506–6511, https://doi.org/10.1073/pnas.1711842115, 2018.

Bell, E., Lamminmäki, T., Alneberg, J., Qian, C., Xiong, W., Hettich, R. L., Frutschi, M., and Bernier-Latmani, R.: Active anaerobic methane oxidation and sulfur disproportionation in the deep terrestrial subsurface, The ISME Journal, 16, 1583–1593, https://doi.org/10.1038/s41396-022-01207-w, 2022.

Blake, R. E., Surkov, A. V., Böttcher, M. E., Ferdelman, T. G., and Jørgensen, B. B.: Oxygen isotope composition of dissolved sulfate in deep-sea sediments: Eastern Equatorial Pacific Ocean, in: Proceedings of the Ocean Drilling Program, 201 Scientific Results, vol. 201, edited by: Jørgensen, B. B., D'Hondt, S. L., and Miller, D. J., Ocean Drilling Program, https://doi.org/10.2973/odp.proc.sr.201.116.2006, 2006.

Böttcher, M. E., Bernasconi, S. M., and Brumsack, H.-J.: 32. Carbon, sulfur, and oxygen isotope geochemistry of interstitial waters from the Western Mediterranean, in: Proceedings of the Ocean Drilling Program, 161 Scientific Results, vol. 161, edited by: Zahn, R., Comas, M. C., and Klaus, A., Ocean Drilling Program, https://doi.org/10.2973/odp.proc.sr.161.1999, 1999.

Böttcher, M. E., Ferdelman, T. G., Jørgensen, B. B., Blake, R. E., Surkov, A. V., and Claypool, G. E.: Sulfur isotope fractionation by the deep biosphere within sediments of the Eastern Equatorial Pacific and Peru Margin, in: Proceedings of the Ocean Drilling Program, 201 Scientific Results, vol. 201, edited by: Jørgensen, B. B., D'Hondt, S. L., and Miller, D. J., Ocean Drilling Program, https://doi.org/10.2973/odp.proc.sr.201.109.2006, 2006.

Boudreau, B. P. and Westrich, J. T.: The dependence of bacterial sulfate reduction on sulfate concentration in marine sediments, Geochimica et Cosmochimica Acta, 48, 2503–2516, https://doi.org/10.1016/0016-7037(84)90301-6, 1984.

Bradley, A. S., Leavitt, W. D., Schmidt, M., Knoll, A. H., Girguis, P. R., and Johnston, D. T.: Patterns of sulfur isotope fractionation during microbial sulfate reduction, Geobiology, 14, 91–101, 2016.

Brunner, B., Bernasconi, S. M., Kleikemper, J., and Schroth, M. H.: A model for oxygen and sulfur isotope fractionation in sulfate during bacterial sulfate reduction processes, Geochimica et Cosmochimica Acta, 69, 4773–4785, https://doi.org/10.1016/j.gca.2005.04.017, 2005.

Campbell, K. A., Farmer, J. D., and Des Marais, D.: Ancient hydrocarbon seeps from the Mesozoic convergent margin of California: carbonate geochemistry, fluids and palaeoenvironments, Geofluids, 2, 63–94, https://doi.org/10.1046/j.1468-8123.2002.00022.x, 2002.

Chambers, L. A., Trudinger, P. A., Smith, J. W., and Burns, M. S.: Fractionation of sulfur isotopes by continuous cultures of Desulfovibrio desulfuricans, Canadian Journal of Microbiology, 21, 1602–1607, 1975.

Chivian, D., Brodie, E. L., Alm, E. J., Culley, D. E., Dehal, P. S., DeSantis, T. Z., Gihring, T. M., Lapidus, A., Lin, L.-H., Lowry, S. R., Moser, D. P., Richardson, P. M., Southam, G., Wanger, G., Pratt, L. M., Andersen, G. L., Hazen, T. C., Brockman, F. J., Arkin, A. P., and Onstott, T. C.: Environmental Genomics Reveals a Single-Species Ecosystem Deep Within Earth, Science, 322, 275–278, https://doi.org/10.1126/science.1155495, 2008.

Coplen, T. B.: Discontinuance of SMOW and PDB, Nature, 375, 285, 1995.

Crameri, F., Shephard, G. E., and Heron, P. J.: The misuse of colour in science communication, Nat Commun, 11, https://doi.org/10.1038/s41467-020-19160-7, 2020.

Crockford, P. W., Kunzmann, M., Bekker, A., Hayles, J., Bao, H., Halverson, G. P., Peng, Y., Bui, T. H., Cox, G. M., Gibson, T. M., Wörndle, S., Rainbird, R., Lepland, A., Swanson-Hysell, N. L., Master, S., Sreenivas, B., Kuznetsov, A., Krupenik, V., and Wing, B. A.: Claypool continued: Extending the isotopic record of sedimentary sulfate, Chemical Geology, 513, 200–225, https://doi.org/10.1016/j.chemgeo.2019.02.030, 2019.

Ding, T., Valkiers, S., Kipphardt, H., De Bièvre, P., Taylor, P. D. P., Gonfiantini, R., and Krouse, R.: Calibrated sulfur isotope abundance ratios of three IAEA sulfur isotope reference materials and V-CDT with a reassessment of the atomic weight of sulfur, Geochimica et Cosmochimica Acta, 65, 2433–2437, https://doi.org/10.1016/S0016-7037(01)00611-1, 2001.

Drake, H. and Reiners, P. W.: Thermochronologic perspectives on the deep-time evolution of the deep biosphere, Proc. Natl. Acad. Sci. U.S.A., 118, e2109609118, https://doi.org/10.1073/pnas.2109609118, 2021.

Drake, H., Åström, M. E., Tullborg, E.-L., Whitehouse, M., and Fallick, A. E.: Variability of sulphur isotope ratios in pyrite and dissolved sulphate in granitoid fractures down to 1km depth – Evidence for widespread activity of sulphur reducing bacteria, Geochimica et Cosmochimica Acta, 102, 143–161, https://doi.org/10.1016/j.gca.2012.10.036, 2013.

Drake, H., Åström, M. E., Heim, C., Broman, C., Åström, J., Whitehouse, M., Ivarsson, M., Siljeström, S., and Sjövall, P.: Extreme 13C depletion of carbonates formed during oxidation of biogenic methane in fractured granite, Nat Commun, 6, 7020, https://doi.org/10.1038/ncomms8020, 2015.

Drake, H., Heim, C., Roberts, N. M. W., Zack, T., Tillberg, M., Broman, C., Ivarsson, M., Whitehouse, M. J., and Åström, M. E.: Isotopic evidence for microbial production and consumption of methane in the upper continental crust throughout the Phanerozoic eon, Earth and Planetary Science Letters, 470, 108–118, https://doi.org/10.1016/j.epsl.2017.04.034, 2017.

Drake, H., Whitehouse, M. J., Heim, C., Reiners, P. W., Tillberg, M., Hogmalm, K. J., Dopson, M., Broman, C., and Åström, M. E.: Unprecedented ^{34}S-enrichment of pyrite formed following microbial sulfate reduction in fractured crystalline rocks, Geobiology, 16, 556–574, https://doi.org/10.1111/gbi.12297, 2018.

Drake, H., Roberts, N. M. W., Reinhardt, M., Whitehouse, M., Ivarsson, M., Karlsson, A., Kooijman, E., and Kielman-Schmitt, M.: Biosignatures of ancient microbial life are present across the igneous crust of the Fennoscandian shield, Commun Earth Environ, 2, 102, https://doi.org/10.1038/s43247-021-00170-2, 2021.

Drake, H., Makahnouk, W. R. M., Roberts, N. M. W., Reinhardt, M., Henkemans, E., Frape, S. K., Tullborg, L., Broman, C., Whitehouse, M. J., and Kooijman, E.: Late Cretaceous and Early Paleogene Fluid Circulation and Microbial Activity in Deep Fracture Networks of the Precambrian Basement of Western Greenland, Geochemistry, Geophysics, Geosystems, 25, e2024GC011646, 2024.

Ester, M., Kriegel, H.-P., Sander, J., and Xu, X.: A Density-Based Algorithm for Discovering Clusters in Large Spatial Databases with Noise, in: Proceedings ACM SIGKDD, Second International Conference on Knowledge Discovery and Data Mining, 266–231, 1996.

Farquhar, J., Johnston, D. T., Wing, B. A., Habicht, K. S., Canfield, D. E., Airieau, S., and Thiemens, M. H.: Multiple sulphur isotopic interpretations of biosynthetic pathways: implications for biological signatures in the sulphur isotope record, Geobiology, 1, 27–36, https://doi.org/10.1046/j.1472-4669.2003.00007.x, 2003.

Feng, D., Chen, D., Peckmann, J., and Bohrmann, G.: Authigenic carbonates from methane seeps of the northern Congo fan: Microbial formation mechanism, Marine and Petroleum Geology, 27, 748–756, https://doi.org/10.1016/j.marpetgeo.2009.08.006, 2010.

Fichtner, V., Kirchner, F., Kutzschbach, M., Strauss, H., Tillberg, M., Whitehouse, M., and Drake, H.: Microscale δ^{34}S and δ^{18}O variations of barite as an archive for fluid mixing and microbial sulphur metabolisms in igneous rock aquifers, Isotopes in Environmental and Health Studies, 1–28, https://doi.org/10.1080/10256016.2024.2410293, 2024.

Fichtner, V., Genske, F., Kooijman, E., and Drake, H.: Carbonate-Associated Sulfate Does Not Record Superheavy δ^{34} S in Deep Scandinavian Bedrock Fractures: Implications for Pyrite Formation in the Deep Biosphere, Geochem Geophys Geosyst, 27, e2025GC012798, https://doi.org/10.1029/2025GC012798, 2026.

Fritz, P., Basharmal, G. M., Drimmie, R. J., Ibsen, J., and Qureshi, R. M.: Oxygen isotope exchange between sulphate and water during bacterial reduction of sulphate, Chemical Geology: Isotope Geoscience section, 79, 99–105, https://doi.org/10.1016/0168-9622(89)90012-2, 1989.

Glossner, A. W., Gallagher, L. K., Landkamer, L., Figueroa, L., Munakata-Marr, J., and Mandernack, K. W.: Factors controlling the co-occurrence of microbial sulfate reduction and methanogenesis in coal bed reservoirs, International Journal of Coal Geology, 165, 121–132, https://doi.org/10.1016/j.coal.2016.08.012, 2016.

Göhring, A., Mauder, M., Kröger, P., and Grupe, G.: Using Gaussian Mixture Model clustering for multi-isotope analysis of archaeological fish bones for palaeobiodiversity studies, Rapid Comm Mass Spectrometry, 30, 1349–1360, https://doi.org/10.1002/rcm.7573, 2016.

Griffith, E. M. and Paytan, A.: Barite in the ocean – occurrence, geochemistry and palaeoceanographic applications, Sedimentology, 59, 1817–1835, https://doi.org/10.1111/j.1365-3091.2012.01327.x, 2012.

Gustafsson, J. and Drake, H.: Biosignatures of an ancient bedrock- and impact structure-hosted deep biosphere: current knowledge and future perspectives, Discov Geosci, 3, 68, https://doi.org/10.1007/s44288-025-00176-9, 2025.

Habicht, K. S., Gade, M., Thamdrup, B., Berg, P., and Canfield, D. E.: Calibration of Sulfate Levels in the Archean Ocean, Science, 298, 2372–2374, 2002.

Halevy, I., Fike, D. A., Pasquier, V., Bryant, R. N., Wenk, C. B., Turchyn, A. V., Johnston, D. T., and Claypool, G. E.: Sedimentary parameters control the sulfur isotope composition of marine pyrite, Science, 382, 946–951, https://doi.org/10.1126/science.adh1215, 2023.

Hallbeck, L. and Pedersen, K.: Explorative analyses of microbes, colloids, and gases together with microbial modelling – Site description model SDM-Site Laxemar, R-08-109, Swedish Nuclear Fuel and Waste Management Co. (SKB), 2008.

Han, T., Bao, H., Peng, Y., Lu, Z., and Song, Y.: The barite record of the past seawater oxygen isotope composition, Nat Commun, 16, 5018, https://doi.org/10.1038/s41467-025-60309-z, 2025.

Heinonen, A., Andersen, T., Rämö, O. T., and Whitehouse, M.: The source of Proterozoic anorthosite and rapakivi granite magmatism: evidence from combined *in situ* Hf–O isotopes of zircon in the Ahvenisto complex, southeastern Finland, JGS, 172, 103–112, https://doi.org/10.1144/jgs2014-013, 2015.

Herlambang, A., John, C. M., and Drake, H.: Physicochemical Conditions of the Devonian-Jurassic Continental Deep Biosphere Tracked by Carbonate Clumped Isotope Temperatures of Granite-Hosted Carbonate Veins, Geofluids, 2023, 1–10, https://doi.org/10.1155/2023/8445328, 2023.

Hoehler, T. M. and Jørgensen, B. B.: Microbial life under extreme energy limitation, Nat Rev Microbiol, 11, 83–94, https://doi.org/10.1038/nrmicro2939, 2013.

Ivarsson, M., Drake, H., Neubeck, A., Sallstedt, T., Bengtson, S., Roberts, N. M. W., and Rasmussen, B.: The fossil record of igneous rock, Earth-Science Reviews, 210, 103342, https://doi.org/10.1016/j.earscirev.2020.103342, 2020.

Iversen, N. and Jorgensen, B. B.: Anaerobic methane oxidation rates at the sulfate-methane transition in marine sediments from Kattegat and Skagerrak (Denmark)1, Limnology & Oceanography, 30, 944–955, https://doi.org/10.4319/lo.1985.30.5.0944, 1985.

Jørgensen, B. B., Böttcher, M. E., Lüschen, H., Neretin, L. N., and Volkov, I. I.: Anaerobic methane oxidation and a deep H2S sink generate isotopically heavy sulfides in Black Sea sediments, Geochimica et Cosmochimica Acta, 68, 2095–2118, https://doi.org/10.1016/j.gca.2003.07.017, 2004.

Jørgensen, B. B., Findlay, A. J., and Pellerin, A.: The Biogeochemical Sulfur Cycle of Marine Sediments, Front. Microbiol., 10, 849, https://doi.org/10.3389/fmicb.2019.00849, 2019.

Kieft, T. L., Walters, C. C., Higgins, M. B., Mennito, A. S., Clewett, C. F. M., Heuer, V., Pullin, M. J., Hendrickson, S., Van Heerden, E., Sherwood Lollar, B., Lau, M. C. Y., and Onstott, T. C.: Dissolved organic matter compositions in 0.6–3.4 km deep fracture waters, Kaapvaal Craton, South Africa, Organic Geochemistry, 118, 116–131, https://doi.org/10.1016/j.orggeochem.2018.02.003, 2018.

Kotelnikova, S.: Microbial production and oxidation of methane in deep subsurface, Earth-Science Reviews, 58, 367–395, https://doi.org/10.1016/S0012-8252(01)00082-4, 2002.

Küsel, K. and Dopson, M.: Groundwater microbial communities across the terrestrial subsurface, Nat Microbiol, 11, 2088–2097, https://doi.org/10.1038/s41564-026-02427-y, 2026.

Laaksoharju, M., Smellie, J., Tullborg, E.-L., Gimeno, M., Hallbeck, L., Molinero, J., and Waber, N.: Bedrock hydrogeochemistry Forsmark- Site descriptive modelling - SDM-Site Forsmark, R-08-47, Swedish Nuclear Fuel and Waste Management Co. (SKB), Stockholm, Sweden, 2008.

Leavitt, W. D., Halevy, I., Bradley, A. S., and Johnston, D. T.: Influence of sulfate reduction rates on the Phanerozoic sulfur isotope record, Proc. Natl. Acad. Sci. U.S.A., 110, 11244–11249, https://doi.org/10.1073/pnas.1218874110, 2013.

Lin, Z., Wang, Q., Feng, D., Liu, Q., and Chen, D.: Post-depositional origin of highly 13C-depleted carbonate in the Doushantuo cap dolostone in South China: Insights from petrography and stable carbon isotopes, Sedimentary Geology, 242, 71–79, https://doi.org/10.1016/j.sedgeo.2011.10.009, 2011.

Liseroudi, M. H., Ardakani, O. H., Pedersen, P. K., Stern, R. A., Wood, J. M., and Sanei, H.: Microbial and thermochemical controlled sulfur cycle in the Early Triassic sediments of the Western Canadian Sedimentary Basin, Journal of the Geological Society, 178, jgs2020-175, https://doi.org/10.1144/jgs2020-175, 2021.

Lyons, Wm. B. and Gaudette, H. E.: Sulfate reduction and the nature of organic matter in estuarine sediments, Organic Geochemistry, 1, 151–155, https://doi.org/10.1016/0146-6380(79)90003-2, 1979.

Machel, H. G.: Bacterial and thermochemical sulfate reduction in diagenetic settings - old and new insights, Sedimentary Geology, 140, 143–175, 2001.

Magnabosco, C., Lin, L.-H., Dong, H., Bomberg, M., Ghiorse, W., Stan-Lotter, H., Pedersen, K., Kieft, T. L., Van Heerden, E., and Onstott, T. C.: The biomass and biodiversity of the continental subsurface, Nature Geosci, 11, 707–717, https://doi.org/10.1038/s41561-018-0221-6, 2018.

McMahon, S. and Parnell, J.: Weighing the deep continental biosphere, FEMS Microbiol Ecol, 87, 113–120, https://doi.org/10.1111/1574-6941.12196, 2014.

McMahon, S. and Parnell, J.: The deep history of Earth's biomass, JGS, 175, 716–720, https://doi.org/10.1144/jgs2018-061, 2018.

Mizutani, Y. and Rafter, T. A.: Isotopic behaviour of sulphate oxygen in the bacterial reduction of sulphate, Geochemical Journal, 6, 183–191, 1973.

Natalicchio, M., Birgel, D., Dela Pierre, F., Martire, L., Clari, P., Spötl, C., and Peckmann, J.: Polyphasic carbonate precipitation in the shallow subsurface: Insights from microbially-formed authigenic carbonate beds in upper Miocene sediments of the Tertiary Piedmont Basin (NW Italy), Palaeogeography, Palaeoclimatology, Palaeoecology, 329–330, 158–172, https://doi.org/10.1016/j.palaeo.2012.02.026, 2012.

Pallud, C. and Van Cappellen, P.: Kinetics of microbial sulfate reduction in estuarine sediments, Geochimica et Cosmochimica Acta, 70, 1148–1162, https://doi.org/10.1016/j.gca.2005.11.002, 2006.

Pasquier, V., Marin-Carbonne, J., Giunta, T., Ruffine, L., and Halevy, I.: Microscale iron and sulphur isotopic compositions reveal pyritization pathways during early diagenesis, Commun Earth Environ, 6, 248, https://doi.org/10.1038/s43247-025-02213-4, 2025.

Paytan, A., Kastner, M., Campbell, D., and Thiemens, M. H.: Sulfur Isotopic Composition of Cenozoic Seawater Sulfate, Science, 282, 1459–1462, https://doi.org/10.1126/science.282.5393.1459, 1998.

Paytan, A., Mearon, S., Cobb, K., and Kastner, M.: Origin of marine barite deposits: Sr and S isotope characterization, Geol, 30, 747, https://doi.org/10.1130/0091-7613(2002)030%3C0747:OOMBDS%3E2.0.CO;2, 2002.

Pedersen, K., Ekendahl, S., Tullborg, E.-L., Furnes, H., Thorseth, I., and Tumyr, O.: Evidence of ancient life at 207 m depth in a granitic aquifer, Geology, 25, 827–830, 1997.

Pedregosa, F., Varoquaux, G., Gramfort, A., Michel, V., Thirion, B., Grisel, O., Blondel, M., Prettenhofer, P., Weiss, R., Dubourg, V., Vanderplas, J., Passos, A., Brucher, M., Perrot, M., and Duchesnay, É.: Scikit-learn: Machine Learning in Python, Journal of Machine Learning Research, 12, 2825–2830, 2011.

Reitner, J., Peckmann, J., Reimer, A., Schumann, G., and Thiel, V.: Methane-derived carbonate build-ups and associated microbial communities at cold seeps on the lower Crimean shelf (Black Sea), Facies, 51, 66–79, https://doi.org/10.1007/s10347-005-0059-4, 2005.

Ries, J. B., Fike, D. A., Pratt, L. M., Lyons, T. W., and Grotzinger, J. P.: Superheavy pyrite (δ34Spyr > δ34SCAS) in the terminal Proterozoic Nama Group, southern Namibia: A consequence of low seawater sulfate at the dawn of animal life, Geology, 37, 743–746, https://doi.org/10.1130/G25775A.1, 2009.

Rubin-Blum, M., Antler, G., Turchyn, A. V., Tsadok, R., Goodman-Tchernov, B. N., Shemesh, E., Austin, J. A., Coleman, D. F., Makovsky, Y., Sivan, O., and Tchernov, D.: Hydrocarbon-related microbial processes in the deep sediments of the Eastern Mediterranean Levantine Basin, FEMS Microbiol Ecol, 87, 780–796, https://doi.org/10.1111/1574-6941.12264, 2014.

Rudnicki, M. D., Elderfield, H., and Spiro, B.: Fractionation of sulfur isotopes during bacterial sulfate reduction in deep ocean sediments at elevated temperatures, Geochimica et Cosmochimica Acta, 65, 777–789, https://doi.org/10.1016/S0016-7037(00)00579-2, 2001.

Ruff, S. E., De Angelis, I. H., Mullis, M., Payet, J. P., Magnabosco, C., Lloyd, K. G., Sheik, C. S., Steen, A. D., Shipunova, A., Morozov, A., Reese, B. K., Bradley, J. A., Lemonnier, C., Schrenk, M. O., Joye, S. B., Huber, J. A., Probst, A. J., Morrison, H. G., Sogin, M. L., Ladau, J., and Colwell, F.: A global comparison of surface and

subsurface microbiomes reveals large-scale biodiversity gradients, and a marine-terrestrial divide, Sci. Adv., 10, eadq0645, https://doi.org/10.1126/sciadv.adq0645, 2024.

Runge, E. A., Mansor, M., Kappler, A., and Duda, J.-P.: Microbial biosignatures in ancient hydrothermal sulfides, Geobiology, 21, 355–377, 2023.

Sela-Adler, M., Ronen, Z., Herut, B., Antler, G., Vigderovich, H., Eckert, W., and Sivan, O.: Co-existence of Methanogenesis and Sulfate Reduction with Common Substrates in Sulfate-Rich Estuarine Sediments, Front. Microbiol., 8, 766, https://doi.org/10.3389/fmicb.2017.00766, 2017.

Sim, M. S., Bosak, T., and Ono, S.: Large Sulfur Isotope Fractionation Does Not Require Disproportionation, Science, 333, 74–77, https://doi.org/10.1126/science.1205103, 2011.

Stevens, T. O. and McKinley, J. P.: Lithoautotrophic Microbial Ecosystems in Deep Basalt Aquifers, Science, 270, 450–455, https://doi.org/10.1126/science.270.5235.450, 1995.

Strauss, H.: The isotopic composition of sedimentary sulfur through time, Palaeogeography, Palaeoclimatology, Palaeoecology, 132, 97–118, 1997.

Takai, K., Nakamura, K., Toki, T., Tsunogai, U., Miyazaki, M., Miyazaki, J., Hirayama, H., Nakagawa, S., Nunoura, T., and Horikoshi, K.: Cell proliferation at 122°C and isotopically heavy CH_4 production by a hyperthermophilic methanogen under high-pressure cultivation, Proc. Natl. Acad. Sci. U.S.A., 105, 10949–10954, https://doi.org/10.1073/pnas.0712334105, 2008.

Torres, M. E., Brumsack, H. J., Bohrmann, G., and Emeis, K. C.: Barite fronts in continental margin sediments: a new look at barium remobilization in the zone of sulfate reduction and formation of heavy barites in diagenetic fronts, Chemical Geology, 127, 125–139, https://doi.org/10.1016/0009-2541(95)00090-9, 1996.

Turchyn, A. V. and Schrag, D. P.: Oxygen Isotope Constraints on the Sulfur Cycle over the Past 10 Million Years, Science, 303, 2004–2007, https://doi.org/10.1126/science.1092296, 2004.

Turchyn, A. V. and Schrag, D. P.: Cenozoic evolution of the sulfur cycle: Insight from oxygen isotopes in marine sulfate, Earth and Planetary Science Letters, 241, 763–779, https://doi.org/10.1016/j.epsl.2005.11.007, 2006.

Valentine, B., Kamenov, G. D., Kenoyer, J. M., Shinde, V., Mushrif-Tripathy, V., Otarola-Castillo, E., and Krigbaum, J.: Evidence for Patterns of Selective Urban Migration in the Greater Indus Valley (2600-1900 BC): A Lead and Strontium Isotope Mortuary Analysis, PLOS ONE, 10, e0123103, https://doi.org/10.1371/journal.pone.0123103, 2015.

Westrich, J. T. and Berner, R. A.: The role of sedimentary organic matter in bacterial sulfate reduction: The G model tested, Limnology and Oceanography, 29, 236–249, https://doi.org/10.4319/lo.1984.29.2.0236, 1984.

Whitehouse, M. J.: Multiple Sulfur Isotope Determination by SIMS : Evaluation of Reference Sulfides for Δ^{33} S with Observations and a Case Study on the Determination of Δ^{36} S, Geostandard Geoanalytic Res, 37, 19–33, https://doi.org/10.1111/j.1751-908X.2012.00188.x, 2013.

Whiticar, M. J.: Carbon and hydrogen isotope systematics of bacterial formation and oxidation of methane, Chemical Geology, 161, 291–314, https://doi.org/10.1016/S0009-2541(99)00092-3, 1999.

Wing, B. A. and Halevy, I.: Intracellular metabolite levels shape sulfur isotope fractionation during microbial sulfate respiration, Proc. Natl. Acad. Sci. U.S.A., 111, 18116–18125, https://doi.org/10.1073/pnas.1407502111, 2014.

Wood, R. S., Lepland, A., Ogliore, R. C., Houghton, J., and Fike, D. A.: Microscale δ34S heterogeneities in cold seep barite record variable methane flux off the Lofoten-Vesterålen Continental Margin, Norway, Earth and Planetary Science Letters, 574, 117164, https://doi.org/10.1016/j.epsl.2021.117164, 2021.

Wortmann, U. G., Bernasconi, S. M., and Böttcher, M. E.: Hypersulfidic deep biosphere indicates extreme sulfur isotope fractionation during single-step microbial sulfate reduction, Geol, 29, 647, https://doi.org/10.1130/0091-7613(2001)029%3C0647:HDBIES%3E2.0.CO;2, 2001.

Wortmann, U. G., Chernyavsky, B., Bernasconi, S. M., Brunner, B., Böttcher, M. E., and Swart, P. K.: Oxygen isotope biogeochemistry of pore water sulfate in the deep biosphere: Dominance of isotope exchange reactions with ambient water during microbial sulfate reduction (ODP Site 1130), Geochimica et Cosmochimica Acta, 71, 4221–4232, https://doi.org/10.1016/j.gca.2007.06.033, 2007.

Wu, X., Holmfeldt, K., Hubalek, V., Lundin, D., Åström, M., Bertilsson, S., and Dopson, M.: Microbial metagenomes from three aquifers in the Fennoscandian shield terrestrial deep biosphere reveal metabolic partitioning among populations, The ISME Journal, 10, 1192–1203, https://doi.org/10.1038/ismej.2015.185, 2016.

Yang, L. W., Yang, T., Li, J., Lin, Y., and Ling, H.-F.: The marine redox evolution and the formation model for the early Cambrian Gongxi-Tianzhu barite deposits in the South China Block, Ore Geology Reviews, 158, 105502, https://doi.org/10.1016/j.oregeorev.2023.105502, 2023.

York, D., Evensen, N. M., Martínez, M. L., and De Basabe Delgado, J.: Unified equations for the slope, intercept, and standard errors of the best straight line, American Journal of Physics, 72, 367–375, https://doi.org/10.1119/1.1632486, 2004.

Zaback, D. A., Pratt, L. M., and Hayes, J. M.: Transport and reduction of sulfate and immobilization of sulfide in marine black shales, Geol, 21, 141, https://doi.org/10.1130/0091-7613(1993)021%3C0141:TAROSA%3E2.3.CO;2, 1993.

Zan, B., Mou, C., Lash, G. G., Yan, J., and Hou, Q.: Diagenetic barite-calcite-pyrite nodules in the Silurian Longmaxi Formation of the Yangtze Block, South China: A plausible record of sulfate-methane transition zone movements in ancient marine sediments, Chemical Geology, 595, 120789, https://doi.org/10.1016/j.chemgeo.2022.120789, 2022.

Zhou, X., Chen, D., Dong, S., Zhang, Y., Guo, Z., Wei, H., and Yu, H.: Diagenetic barite deposits in the Yurtus Formation in Tarim Basin, NW China: Implications for barium and sulfur cycling in the earliest Cambrian, Precambrian Research, 263, 79–87, https://doi.org/10.1016/j.precamres.2015.03.006, 2015.